HYPERSONIC SHAPE PARAMETERIZATION USING CLASS – SHAPE TRANSFORMATION WITH STAGNATION POINT HEAT FLUX

A Dissertation
Presented to
The Academic Faculty

by

Justin H. Fan

In Partial Fulfillment
of the Requirements for the Degree
Master of Science in the
Guggenheim School of Aerospace Engineering

Georgia Institute of Technology
May 2019

HYPERSONIC SHAPE PARAMETERIZATION USING CLASS – SHAPE TRANSFORMATION WITH STAGNATION POINT HEAT FLUX

Approved by:

Dr. Dimitri Mavris, Advisor
Guggenheim School of Aerospace Engineering
Georgia Institute of Technology

Dr. Bradford Robertson
Guggenheim School of Aerospace Engineering
Georgia Institute of Technology

Dr. Henry Schwartz
Guggenheim School of Aerospace Engineering
Georgia Institute of Technology

Date Approved: April 26, 2019

I dedicate this thesis to David A. Fox. Thank you for showing me the beauty in flight and helping me realize a passion in aerospace and engineering.

ACKNOWLEDGEMENTS

When I first entered the engineering field in the fall of 2013 to pursue a Bachelor's degree in Mechanical Engineering, I never would have that I would present a Master's thesis at Georgia Institute of Technology. After becoming fascinated with aerospace during junior design projects, the past four years have been filled with spectacular opportunities to learn and become engaged with the aerospace field.

Foremost, I would like to express my sincere gratitude to my advisor Dr. Dimitri Mavris for extending the opportunity to study Aerospace Engineering in the Aerospace Systems Design Laboratory at Georgia Institute of Technology. His guidance and support in the Aerospace Systems Design Laboratory has led to growth in knowledge and skill as well as development as an individual. The numerous research areas and networking opportunities fostered curiosity in the realm of hypersonics which have ultimately led to this thesis.

I would also like to thank members of my thesis committee, Dr. Bradford Robertson and Dr. Henry Schwartz. Their technical support, enthusiasm about hypersonics, and encouragement helped immensely throughout the thesis process.

I would like to thank my family for their unconditional love and support throughout these two years of graduate school. Finally, I would like to thank coworkers and friends that I have met during my time at ASDL and Georgia Institute of Technology. Thank you all for accompanying me along this journey.

TABLE OF CONTENTS

LIST OF TABLES

LIST OF FIGURES

SUMMARY

Hypersonic vehicles are no longer just an idea that occasionally draws funding and research attention from industry and military. With an ever-increasing desire to understand and realize high speed flight, hypersonic flight is the new focus in attempt to reduce travel time, gain access to space, and enhance global defense capabilities. Hypersonic vehicle research and development has historically and is still primarily isolated to the defense industry and select collaborations in the academic field. It serves to greatly benefit the general hypersonic research and development community for academic research tools to be at state-of-the-art level.

While much of hypersonic research, development, and data is highly proprietary, the hypersonics community has been able to produce air-breathing, two-dimensional generic hypersonic vehicle (GHV) configurations and waverider geometries. Given the difficulty of the hypersonic flight regime, there are regions of the vehicle design that are not well modeled. Hypersonics research and development was previously limited by insufficient computational capabilities, which could only capture a portion of the vehicle's flight performance characteristics. However, now with enhanced computational analysis tools, the models to which the tools are applied must also be improved to keep pace. As such, much of hypersonics attention is now directed towards hypersonic glide vehicles (HGV).

Unlike design of subsonic aircraft, a hypersonic system cannot be optimized strictly for a single design parameter or performance characteristic. For this reason, there are still a lot of uncertainties in the hypersonics design process. The uncertainties stem from the extremely tight coupling between aerodynamics, aerodynamic heating, structures, controls,

trajectory, and mass properties. As a result, there are gaps in the ability to analyze a hypersonic vehicle that simultaneously captures the critical components of the relevant disciplines. Aerodynamic heating is a region of interest because its effects can heavily impact the other design disciplines. Aerodynamic heating effects are often only accounted for through the application of computational fluid dynamics (CFD). Unfortunately, the process of analyzing aerodynamic heating with CFD and then modifying the geometry is computationally expensive. Recent work has provided shape parameterization methods that are analytical and allow direct control of geometry changes. Incorporating these methods with existing stagnation point heat flux equations may allow for geometric changes earlier in the design process, thereby accounting for an aspect of aerodynamic heating further upstream in the geometry generation process. Thus, the purpose of this thesis is to develop a shape parameterization approach to generate parametric three-dimensional vehicle geometries with the inclusion of aerodynamic heating.

CHAPTER 1: INTRODUCTION

The hypersonic flight regime is an incredibly exciting yet extremely daunting design area to explore. There have been many efforts towards hypersonic develop from intercontinental ballistic missiles to space re-entry vehicles such as the Apollo vehicles. While much of hypersonics development has been done and continues in the space domain, atmospheric hypersonics has only recently been given a jumpstart. In the 1950s, a class of hypersonic vehicles was developed by Nonweiler by the name of waverider. [1] Within the realm of atmospheric hypersonic vehicles, waverider geometries are one of the most popular configurations for hypersonic air-breathing and boost-glide systems. Waverider geometries are of particular interest due to high aerodynamic performance which is especially useful for HGV. Throughout hypersonic research, many vehicles have been designed to have a similar geometry as the waverider in order to capture the aerodynamic performance. A shape parameterization method that has been used to model vehicles similar to the waverider is the Class-Shape Transformation (CST) method. [2] Simultaneously, while the waverider concept was in development, Allen and Eggers discovered that blunt bodies would be better in preventing the nose of ICBMs from melting. It was found that the maximum value of heat transfer is inversely proportional to the square root of the leading-edge radius. [3] [4] [5] Provided that the CST method is capable of modeling hypersonic vehicle geometries, this thesis aims to use the CST method to design hypersonic geometries with the aerodynamic heating effects.

1.1 Hypersonics

Through decades of aircraft and spacecraft design, traveling at ever increasing speeds has always been a long-running objective. Within the realm of supersonic air-breathing vehicles, there has been the Concorde, a supersonic transport vehicle and the SR-71, a supersonic stealth reconnaissance aircraft. Beyond supersonic speeds, there is the subsequent flight regime of hypersonic speeds which is generally classified as traveling at speeds greater than Mach 5. The first vehicle to achieve hypersonic flight was a WAC Corporal boosted by a German V-2 rocket, which reached maximum velocity of just over 5000 mph. [6] In the decades to follow, numerous hypersonic vehicles have emerged such as the X-43, X-51, Apollo mission capsules, and space shuttles. For the space shuttle and Apollo capsules, re-entry velocities reached Mach 25 all the way to Mach 36. [7]

As design and analysis tools have progressed, hypersonics research and development have been revitalized. The surge is fueled in large part due to foreign powers, such as China and Russia, developing and testing hypersonic technologies. According to the *Business Insider*, the US Air Force has already awarded contracts to develop these new capabilities. [8] While foreign powers have tested capabilities, it is suspected that the hypersonic vehicles will not be deployed for another 3-5 years. The vehicles are of great concern because they travel at such high speeds that it becomes difficult to track and intercept. Previously, hypersonic technology development has been hindered due to fluctuations in investment and deficiencies in computational tools to perform the necessary analyses.

Now with near billion-dollar development contracts being awarded by the government, companies and academia cannot afford to be wasteful with the massive amount of funding that is being directed towards hypersonics. [9] The development of hypersonic vehicles can directly impact defense capabilities, transport times, and less expensive method to access space.

In the subsonic regime, it is safe to assume that the density of the air is constant when the freestream Mach number is less than or equal to 0.3. Beyond Mach 0.3, flows are considered to be compressible. In the supersonic and hypersonic regime, the flow around an object is characterized by the shock waves that form. Shock waves are pressure waves generated from a body traveling at supersonic speeds. The pressure waves coalesce, forming a large compression wave at the front of a body. An essential aspect of hypersonic flow is the strength of shock waves which causes the boundary layer also grows to be very large around the vehicle surface. In addition, across the shock wave, thin shock layers forms where flow properties change drastically; pressure, density, and temperature increase behind the shock wave while the Mach number decreases. [6] These changes in the flow properties directly affect the lift, drag, pressure, aerodynamic heating, and controllability of the vehicle. The change in various properties shows that the disciplines involved in designing a hypersonic vehicle are highly coupled. Figure 1depicts important components from each of the different flow regimes. [6]

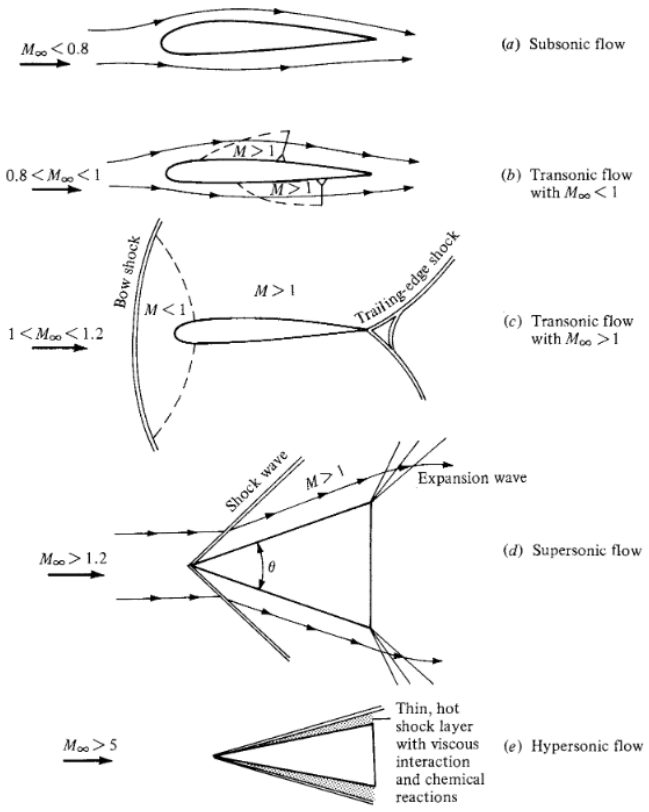

Figure 1: Flow Regimes

Given the revived interest of hypersonics in the defense and aerospace field, it is critical and an urgent task to develop models suitable for high-fidelity analysis. Due to the high level of coupling, hypersonic vehicles are developed around numerous parameters. In the conceptual phase of design, however, it becomes a cumbersome process to account for every design parameter as it can be computationally expensive. As a result, critical relations and parameterizations must be identified to create a parametric model.

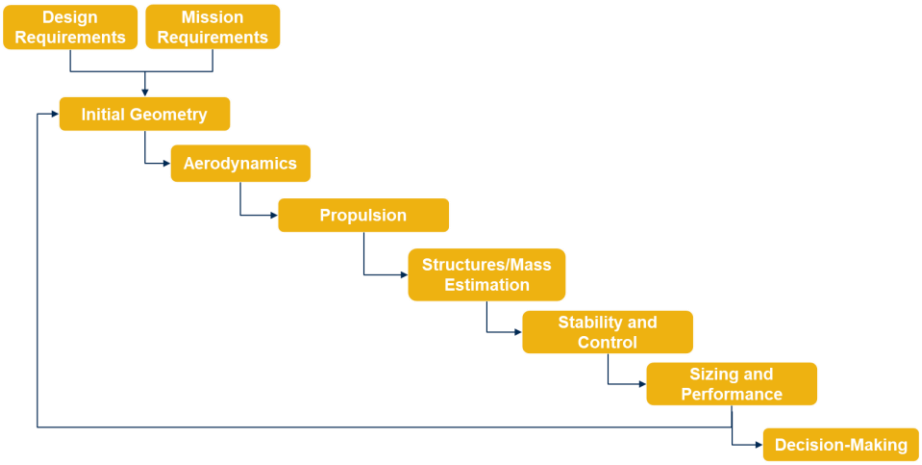

Figure 2: Sequential design process for traditional aircraft

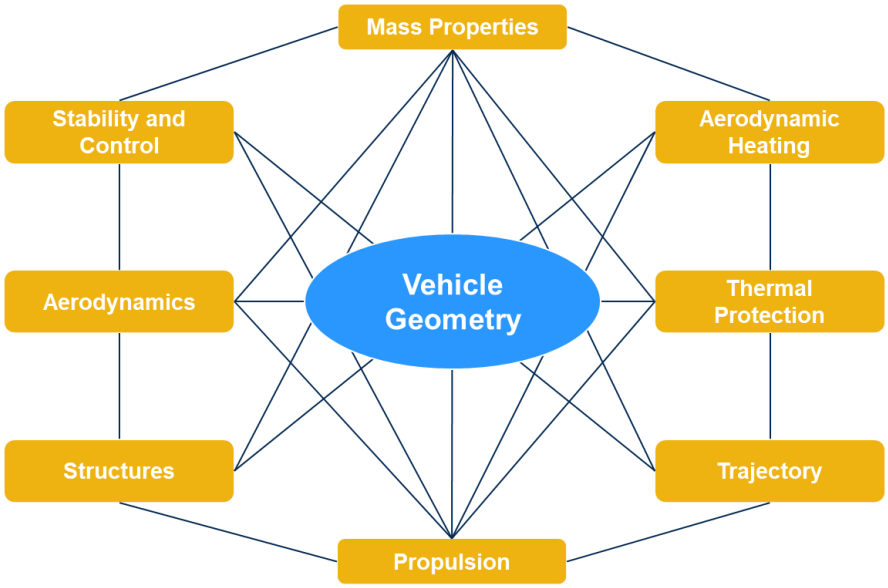

Figure 3: Hypersonic design discipline coupling

Figure 2 depicts a high-level design process for traditional aircraft where only select parameters are sequentially passed through discipline analyses. This is in stark contrast to Figure 3 which shows that disciplines in hypersonic design become heavily dependent on each other.

1.2 Aerodynamic Optimization

Aerodynamic optimization has become a critical component for effective and robust aircraft design. With increasingly complex geometries, geometry development and aerodynamic analysis can no longer be accomplished by using trial and error wind tunnel experiments. For this reason, computational fluid dynamics (CFD) is useful for accurate and quicker analyses of designs with the objective of determining lift and drag performance of geometries.

For a certain set of operating conditions, there may be multiple solutions for the given conditions. Optimization is the process of taking the operating conditions with additional constraints to find the best solution among the many potential solutions. Coupling optimization with aerodynamic analysis permits for the designer to determine the most aerodynamically efficient solution. For hypersonic vehicles, aerodynamically efficient typically indicates maximum lift and minimum drag. Optimization then, allows for exploration of a larger design space to find the best solution for a specific set of conditions. Not only does aerodynamic optimization enable larger design space exploration, but it can usually perform the analyses in a computationally efficient manner.

1.3 Aerodynamic Heating and Efficiency

One of the more dominant couplings at hypersonic speeds is aerodynamic heating and efficiency. An example of the importance of aerodynamic heating is the Space Shuttle Columbia accident that occurred in 2003. [10] The thermal protection system (TPS) material had been damaged in the launch process. Then during the vehicle's re-entry phase, high temperatures and hot gases propagated through the wing structure which resulting in

material failure and disintegration of the entire vehicle. Figure 4 illustrates the location of wing damage spread of high-speed flow and temperatures. [10] This is a major risk factor for hypersonic vehicles and must therefore be considered in the design process. The aerodynamic heating presents a challenge in hypersonic flight as the scaling is proportional to ρM^3 where M is the Mach number. [11] This is also seen later in heat stagnation point heat flux equations.

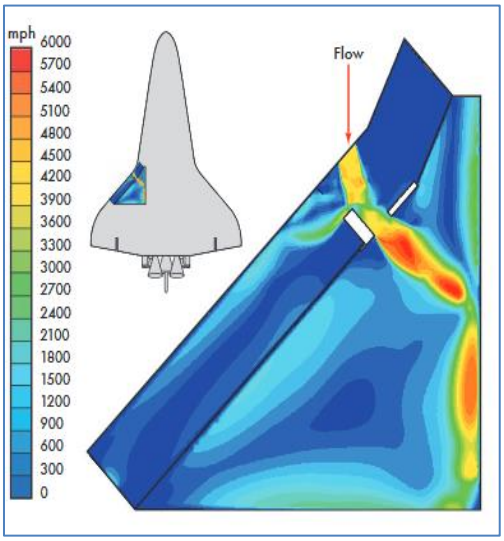

Figure 4: Space Shuttle *Columbia* failure analysis

Through a series of derivations from the heat transfer coefficient known as the Stanton number, it is determined that the total heat input into the vehicle is proportional to the ratio of skin friction drag to total drag. The full derivation of the total heat input can be examined in *Anderson.* To reduce the total heat input, it is better to utilize a blunt body over a sharp and slender body. However, the use of a blunt body means that the overall drag coefficient, C_D, would increase. The increased C_D indicates that the aerodynamic efficiency, often measured by the lift-to-drag ratio, will decrease. Equation 1 is the total heat input for the vehicle where C_f is the skin friction drag coefficient and C_D is the pressure

drag coefficient. For slender bodies, skin friction is more dominant than pressure and so Equation 2 is applied. In contrast, blunt bodies experience more pressure drag and so it can be reasonably assumed that Equation 3 can be applied to total heat input. Applying the increased coefficient of drag assumption to Equation 4 shows that the lift-to-drag ratio would decrease as a result of implementing blunt bodies.

$$\mathrm{Q_{total}} = \frac{1}{2}\left(\frac{C_f}{C_D}\right)\left(\frac{1}{2}mV_E^2\right) \tag{1}$$

$$\frac{C_f}{C_D} \approx 1 \text{ for slender body} \tag{2}$$

$$\frac{C_f}{C_D} \ll 1 \text{ for blunt body} \tag{3}$$

$$\frac{\mathrm{L}}{\mathrm{D}} = \frac{q_\infty S C_L}{q_\infty S C_D} = \frac{C_L}{C_D} \tag{4}$$

It can be concluded from the previously mentioned mathematical relationships that an important tradeoff exists between aerodynamic heating and efficiency. [10]

1.4 Research Objective

As previously mentioned, the presence of aerodynamic heating is an important design factor that affects vehicle structure and flight performance. Therefore, hypersonic shape design can be improved by:

1.4.1 Integrating aerodynamic heating with shape parameterization

Hypersonic vehicles can have sharp and slender, blunt, or a combination of the bodies. The shape of the body holds valuable information that is directly related to the aerodynamic heating that is experienced in hypersonic flight. Consequently, **the objective of this research involves obtaining geometries based on desired heat transfer rates while maintaining optimal lift-to-drag efficiency.**

CHAPTER 2: BACKGROUND

2.1 Shape Parameterization

There have been numerous methods developed to model vehicle geometries. Researchers and analysts face the challenge of choosing which methods shape parameterization methods to use depending on desired application or conditions. Provided that design disciplines are tightly coupled, the selected shape parameterization method should be parametric where vehicles are defined by a manageable amount and meaningful design variables.

2.1.1 Inverse Aerodynamic Design

A unique aspect of supersonic and hypersonic flow is the presence of shock waves. For hypersonic flow, in specific, the oblique shock that is formed on the leading edge lies very close to the surface of the body and can be seen in Figure 5. [6] However, the presence of the shock wave is detrimental to the aerodynamic efficiency of the vehicle because as the freestream Mach number increases, so does the strength of the shock wave which increases wave drag, profile drag, and friction drag. As such, the aerodynamic efficiency which is governed by the maximum lift-do-drag ratio, $(L/D)_{max}$, will decrease significantly. [6] The shock wave that is created by the body provides important information regarding the lift, wave drag, and noise.

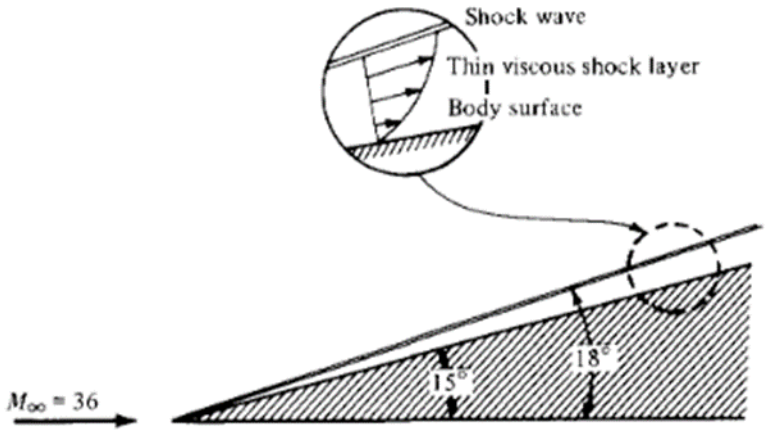

Figure 5: Thin shock layer at hypersonic speeds

A design method that utilizes the information from the shock wave is known as the inverse aerodynamic design method, also known as waverider design. [13] [14] [15] [16] This method utilizes a set freestream Mach number and a deflection angle from the flowfield around an arbitrary wedge. The waverider design methodology follows a process where the vehicle surfaces are enclosed by a designated shockwave geometry, and the leading edges are traced on the shockwave. The advantage of the waverider vehicle shape is that the lift-to-drag ratio is slightly increased from a vehicle that is detached from the shock wave. [6] Examples of waverider geometries are shown in below in Figure 6. [6] [17]

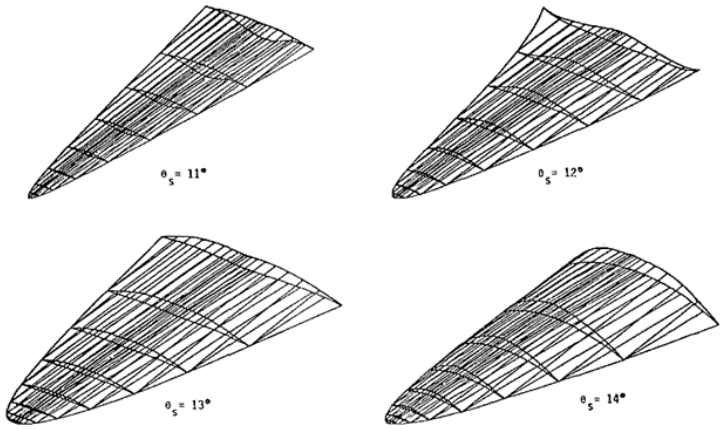

Figure 6: Waverider geometries derived from inverse aerodynamic design

By tracing the leading on the shockwave, it keeps the shockwave attached to the geometry. In doing so, it limits the pressure leak from the bottom surface to the upper surface which would reduce the amount of lift on the vehicle. The increased aerodynamic efficiency for waverider geometries can be seen below in Figure 7. [6]

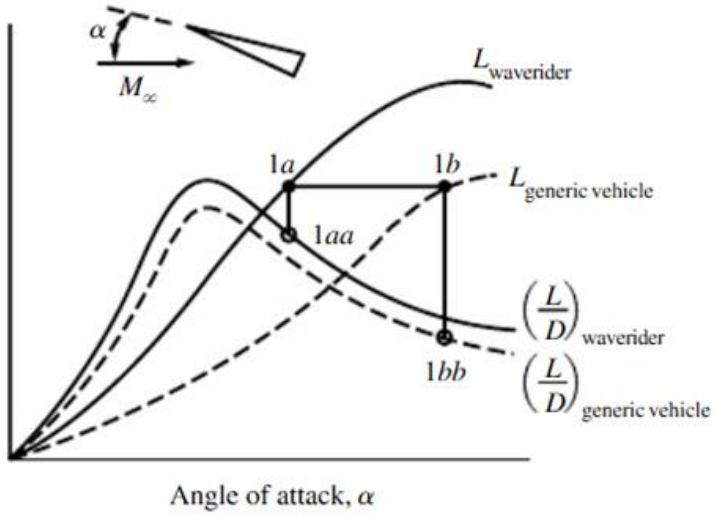

Figure 7: Aerodynamic efficiency comparison for generic and waverider geometries

2.1.2 Class Shape Transformation (CST)

Another method of generating three-dimensional hypersonic vehicles is using the class-shape-transformation (CST) parameterization method. In order to geometrically define any aircraft, Sobieczky states that most aero-vehicle components can be grouped into two basic types of configurations. [13] [14] The first configuration group, wing type shapes or class 1, consists of aircraft wings, helicopter rotors, turbomachinery blades, empennage fins, pylons, struts, and variable airfoils. The second group, the body type shapes or class 2, consists of aircraft fuselages, rotor hubs and shrouds, channels and tubing, axisymmetric bodies, nacelles, containers, and variable cross sections. When considering shapes from both class 1 and 2, many of the geometries tend to have rounded noses or pointed ends. The challenge with the special geometries is that they can only be described mathematically with continuous but nonanalytic functions. Therefore, the class 1 and 2 geometries are then often represented by a cloud of coordinate points. However, the coordinate points are not suitable for the purpose of creating a parametric or optimizable geometry.

The CST method, first developed by *Kulfan and Bussoletti*, is a method in which analytic expressions are developed to represent the geometries that would otherwise encounter singularities. [18] [19] The CST method was initially developed to better represent airfoil geometries. This is achieved by first defining a class function which represents general geometries such as classes of airfoils, axisymmetric bodies, or axisymmetric nacelles. The method then employs shape functions which provides a way to change the general shape to form unique geometries defined by well-behaved analytic function. The shape function allows control over key parameters to create unique

geometries within a class. The class and shape functions are then transformed and represented using Bernstein polynomials. Bernstein polynomials allow the functions to be decomposed into separate component shapes. Following the application for airfoil geometry, the method is expanded to represent three-dimensional shapes.

2.2 Review of Past Research

2.2.1 Examination of parameterization methods and aerodynamic optimization

This effort involved examining three different shape parameterization techniques and comparing performance aspects of the different shape optimization process. [20] The CST method was introduced primarily due to its ability to overcome complex geometric representation from large surface curvature and infinite second derivatives at the leading-edge of airfoils. The CST method was employed to model the geometry of an ONERA M6 wing, a target pressure distribution, and drag minimization. Results from the modelling showed that the CST method was able to model the wing such that the target pressure was capture within acceptable accuracy with a low number of design variables. In the drag minimization test cases, the CST method was also shown to be efficient in drag reduction. Though all the shape parameterization techniques performed well, there is a need to utilize few design variables while still being able to achieve optimized performance properties with acceptable accuracy.

2.2.2 Three-dimensional CST method with aerodynamic optimization

This effort involved using the CST method and its ability to be extended to 3-D. [21] A single class-shape function does not contain the necessary degrees of freedom to

model an entire aircraft geometry. The research by *Hua et al.* highlighted the use of 3D CST to build an aircraft by creating a library of basic components such as the fuselage, wings, and empennage. The aircraft is then formed into one geometry using a component combination method, example aircraft generated with 3D CST can be seen in Figure 8. [21] Using the 3D CST and component combination, the X-33 hypersonic aircraft was modelled and optimized for maximum lift-to-drag with the volume selected as the optimization constraint.

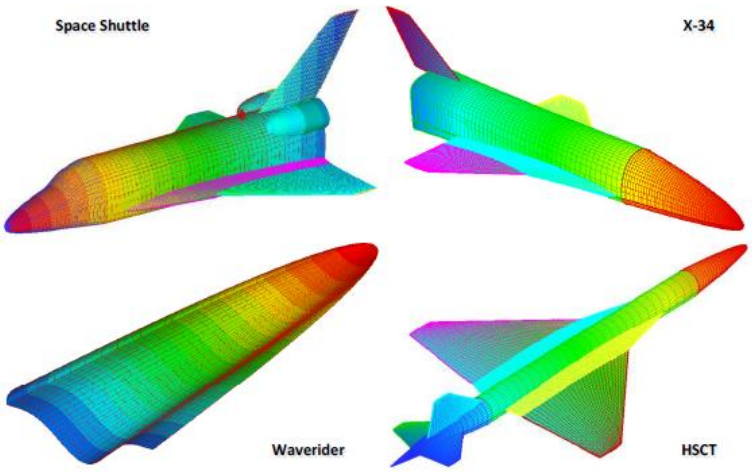

Figure 8: Vehicle geometries generated by combination of 3D CST components

2.2.3 Parameterization and optimization of HGV configurations

This research effort involved implementing the 3D CSRT method to generate an HGV with geometry similar to that of a waverider. [2] The waverider geometry was of particular interest for hypersonic applications due to its aerodynamic performance. The HGV was created by adding more class and shape functions to include additional parameters. For simplicity, the shape functions were set equal to 1. The HGV was then integrated into a multi-objective algorithm to determine the optimal lift-to-drag ratio and

volumetric efficiency. As expected, the results indicated that volumetric efficiency and lift-to-drag ratio conflict and cannot be simultaneously maximized. Figure 9 depicts feasible HGV geometries generated in the research done by *Zhang et* al. [2] Expanding the scope of this research to include other design disciplines such as aerodynamic heating will provide more accurate and robust design options.

Figure 9: Feasible HGV designs

2.3 Summary of Research and Research Gaps

The review of prior research highlights several strengths, limitations, and/or gaps in hypersonic shape parameterization. First, prior research shows that the CST method is a popular and useful method used for vehicle shape parameterization. The research also shows that the CST method can generate geometries fit for hypersonic analysis such as the experimental X-33 aircraft and waverider geometries. Second, all efforts involving the CST method have been integrated with the optimization of volumetric efficiency as well as aerodynamic efficiency. This is particularly important because hypersonics often requires maximum lift-to-drag. An ideal hypersonic geometry would have a very slender profile, but the volume constraints are necessary for instrumentation, cooling, and structural purposes.

There has been plentiful research in using the CST method to generate geometries and then performing aerodynamic and volumetric optimization. It is important to note, however, that most efforts have not included aerodynamic heating. This research aims to address this gap by including an aspect of aerodynamic heat. Ignoring the effects of aerodynamic heating could lead to erroneous or incorrect evaluation of hypersonic geometries. The coupling between aerodynamics and aerodynamic heating has important design; therefore, it is useful to begin including aerodynamic heating into the hypersonics design process.

2.4 Research Questions

The research questions formulated below are motivated by the limitations in the research highlighted in section 2.3 as well as the overarching research objective.

2.4.1 Research Question 1

As discussed in section 2.3, past studies have primarily focused on using the CST to create hypersonic vehicles that are optimized for aerodynamic and volumetric efficiency. Little to no work has been conducted to include aerodynamic heating with the CST hypersonic shape parameterization. Thus, the research question is as follows:

Research Question #1: *How can aerodynamic heating be incorporated into CST hypersonic parameterization?*

2.4.2 Hypothesis 1

The hypothesis for Research Question 1 is:

Hypothesis 1: *If the leading-edge from stagnation point heat flux is linked with the first weight coefficient in the CST method, then aerodynamic heating can be incorporated into CST shape parameterization.*

2.4.3 Research Question 2

As discussed in Chapter 1, there is a trade-off between aerodynamic efficiency and aerodynamic heating. For reduced aerodynamic heating, blunt geometries must be introduced but sharper geometries are preferable for higher aerodynamic efficiency. This leads to the following research question:

Research Question 2: *How will aerodynamic efficiency for 2D airfoils change with heat transfer rates and area constraints?*

CHAPTER 3: TECHNICAL APPROACH

In order to successfully achieve the research objectives and answer the research questions outlined in the previous chapter, it was important to identify and implement an effective method. The following steps provide an overview of the approach:

3.1 Problem Definition

As mentioned in section 1.4, the objective of this research is to:

1. Generate geometries based on desired heat transfer rates while maintaining optimized aerodynamic efficiency

To achieve the objective, there was a need to determine relationship between shape parameterization and heat flux. For this research, the parameter of interest is the leading-edge radius of the airfoil. As it is described in section 3.2.1, a special characteristic of the CST method is the ability to control the shape of the leading-edge radius. Thus, the previously mentioned CST method was selected as the shape parameterization to be linked with aerodynamic heating, specifically stagnation point heat flux.

3.2 Proposed Method

Figure 10 illustrates the proposed method towards obtaining aerodynamically optimized airfoils with stagnation point heat flux.

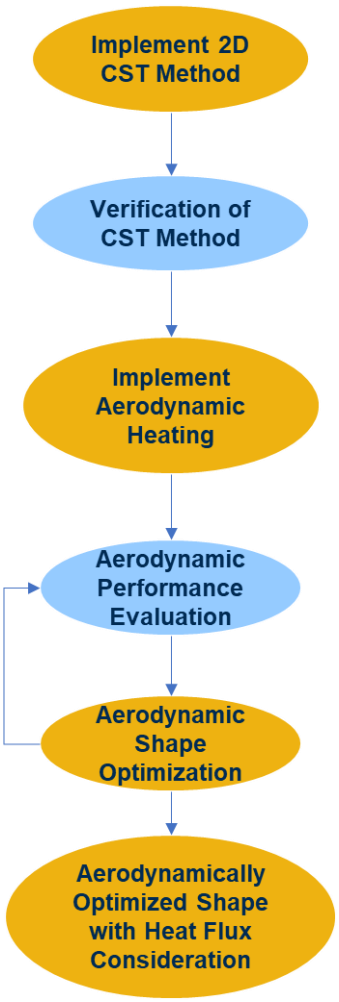

Figure 10: Overview of proposed method

3.2.1 CST Application

The CST method, first developed by *Kulfan*, is a method in which analytic expressions are developed to represent the geometries that would otherwise encounter singularities. [18] The CST method was initially developed as a way to better represent airfoil geometries. This is achieved by first defining a class function which represents general geometries such as classes of airfoils, axisymmetric bodies, or axisymmetric nacelles. The method then employs shape functions which provides a way to change the

general shape to form unique geometries defined by well-behaved analytic function. The shape function allows control over key parameters to create unique geometries within a class. The class and shape functions are then transformed and represented using Bernstein polynomials. Bernstein polynomials allow the functions to be decomposed into separate component shapes. Following the application for airfoil geometry, the method can be expanded to represent three-dimensional shapes.

In two – dimensions, a geometry is expressed with the following mathematical function:

$$\varsigma(\varphi) = C_{N_2}^{N_1}(\varphi)\, S(\varphi) \tag{5}$$

where $\varsigma = z/c$, $\varphi = x/c$, where c is the chord length of a wing. The class of a given curve is defined by N_1 and N_2 in the function below:

$$C_{N_2}^{N_1}(\varphi) = \varphi^{N_1}(1 - \varphi)^{N_2} \tag{6}$$

The shape function is then represented by:

$$S(\varphi) = \sum_{i=0}^{n} b_i \cdot \binom{n}{i} \varphi^i (1-\varphi)^{n-i} \tag{7}$$

where b_i is the location of the control node and $\binom{n}{i}$ are Binomial coefficients. [18] [19] [22]

The shape function is represented as a general Bernstein polynomial, where *n* is the order of the polynomial and b_i is the Bernstein coefficient. Implementing parametric functions,

Cartesian coordinates can be mapped into a new coordinate system of (φ, η). The *x*-direction is mapped axially as:

$$x(\eta) = \eta \tag{8}$$

The y-direction is then mapped as a function of η, resulting in:

$$y(\eta) = C_{T_2}^{T_1}(\eta) \sum_{k=0}^{t} b_k B_t^k(\eta) \tag{9}$$

$$\varphi = \frac{y}{y(\eta)} \tag{10}$$

Here, b_k and B_t^k are the Bernstein polynomial coefficient and basis function, respectively. φ is then the normal coordinate defined as a function of η. The third coordinate that will allow for three dimensions is then mapped as a function of both φ and η: [2] [23]

$$z(\varphi, \eta) = C_{N_2}^{N_1}(\varphi) C_{M_2}^{M_1}(\eta) \sum_{i=0}^{n} \sum_{j=}^{m} b_{i,j} B_n^i(\varphi) B_m^j(\eta) + \Delta\varsigma_{M,N}(\varphi, \eta)|_{upp,low} \tag{11}$$

The CST method is then modified by *Straathof et al* [24] by implementing B-splines as an additional shape function. By doing so, the CST method has more ability to change the geometry locally. This method then becomes the Class-Shape-Refinement-Transformation (CSRT) method. The B-spline is defined as:

$$\boldsymbol{p}(u) = \sum_{i=0}^{n} \boldsymbol{p}_i N_{i,k}(u) \tag{12}$$

where **p** is a vector of control points. The B-splines are now independent of the control points with the basis function $N_{i,k}$. The combined Bernstein polynomials and B-splines class-shape equation that defines the geometry then becomes Equation 13:

$$\varsigma(\varphi,\eta) = C_{N_2}^{N_1}(\varphi) \cdot S(\varphi,\eta) \cdot R(\varphi) \tag{13}$$

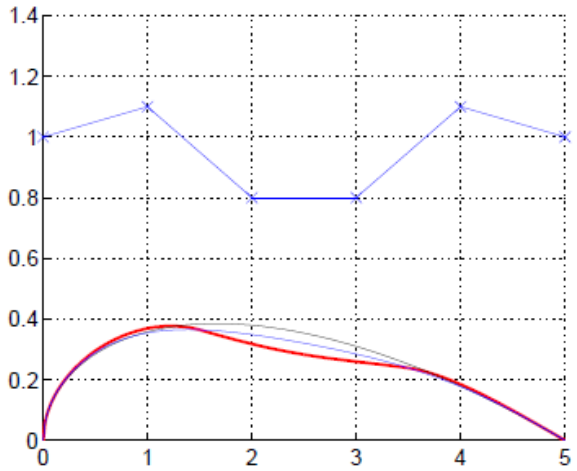

Figure 11: Bernstein polynomial and B-spline shape functions

Figure 11 shows the application of the CST method with Bernstein polynomial and B-spline shape functions. [24] The blue line illustrates shape modification using Bernstein polynomials as shape functions and the red line illustrates the use of B-spline shape functions. Changing one component of the B-spline weight vector leads to very localized change in the geometry. Having only local control is not entirely practical as it would require tedious evaluation to modify the geometry. Therefore, the use of both Bernstein polynomials and B-splines are effective for shape parameterization.

The CST method possesses two special characteristics. When x = 0, the first weight coefficient corresponds directly to the leading-edge radius seen in Equation 14: [18] [19] [25]

$$S(0) = A_0 = \sqrt{\frac{2R_{le}}{c}} \tag{14}$$

Additionally, when x = 1, the last weight coefficient of the Bernstein polynomial corresponds to the trailing-edge boat-tail angle and thickness, as seen in Equation 15: [18] [19] [25]

$$S(1) = \tan\beta + \frac{\Delta Z_{te}}{c} \tag{15}$$

3.2.2 Aerodynamic Heating

The goal for this step is to incorporate aerodynamic heating parameters linked with the vehicle's leading edge. It was previously mentioned that aerodynamic heating becomes a major concern for hypersonic vehicles. As the vehicle travels at increasingly large velocity, the heat buildup and transfer to the vehicle shell could result in the material melting. This is especially true at the leading edge because it is often the location of the stagnation point. Based on boundary-layer equations, dissociative flow, and effects of diffusion and molecular recombination in high speed flight, *Fay and Riddell* were able to develop numerical solutions for the stagnation point equation. [26] [27] [28] [29] [30]The equilibrium heat transfer rate at the stagnation point was computed to be the following Equation 16 and Equation 17:

$$\dot{q}_w = \frac{0.763}{(Pr_w)^{0.6}}(\rho_e\mu_e)^{0.4}(\rho_w\mu_w)^{0.1}[(h_o)_e - h_w]\left[1 + (Le^{0.52} - 1)\frac{h_d}{(h_o)_e}\right]\left[\frac{du_e}{d_x}\right]^{0.5} \quad (16)$$

$$\frac{du_e}{dx} = \frac{1}{R}\sqrt{\frac{2(\rho_e - \rho_\infty)}{\rho_e}} \quad (17)$$

However, the issue with the equations developed by *Fay and Riddell* is that the equation contains parameters that are not easily attainable for initial estimation. The unknown parameters include density and absolute viscosity at the edge of the boundary layer. The Lewis number, *Le*, is dependent on the mass and thermal diffusivity of the flow. Additional aerodynamic heating equations have been derived from boundary-layer theory, laminar, and turbulent convective heating. The general form of the aerodynamic heating is as follows in Equation 18: [31] [32]

$$\dot{q}_w = \frac{dq}{dt} = C\rho^N V^M \quad (18)$$

The values of *C, N,* and *M* vary depending on the application; for aerodynamic heating at the stagnation point, the values for the constant are listed in Table 1. This then results in Equation 19, a stagnation point heat flux equation given by Tauber and Meneses with variables defined in Table 2: [6]

Table 1: Numerical values of aerodynamic heating constants

Stagnation Point Constants		
C	N	M
$1.83E\text{-}8(R)^{-1/2}(1 - g_w)$	0.5	3

$$\dot{q}_w = \rho_\infty^{0.5} V_\infty^3 (1.83 \times 10^{-8} R^{-0.5}) \left(1 - \frac{h_w}{h_o}\right) \quad (19)$$

Table 2: Variable description for Tauber and Meneses heat flux equation

ρ_∞	Freestream density
V_∞	Flight velocity
R	Effective Nose Radius
h_w	Wall enthalpy
h_o	Total enthalpy

From the equation it can be seen that the heat flux or heat transfer per unit area is proportional to the freestream velocity cubed. It can also be seen that the heat flux is inversely proportional to the square root of radius, *R*, of the nose.

Equation 20 – Equation 24 are another set of simplified stagnation point heat flux equations have also been derived by *Sutton-Graves*. [27] [33]

$$\dot{q}_w = k \left(\frac{\rho}{R_n}\right)^{\frac{1}{2}} V^3 \quad (20)$$

where $k = 1.7415 \times 10^{-4}$ when operating in the Earth's atmosphere. [15] K = 3.6×10^{-4} for air in Equation 21 and Equation 23. [33]

$$\dot{q}_{cw} = (H_\infty - H_w)K\sqrt{\frac{P_{st}}{R_{le}}} \tag{21}$$

$$\dot{q}_{cw} = H_\infty K\sqrt{\frac{P_{st}}{R_{le}}} \tag{22}$$

$$\mathrm{H}_\infty = c_p T_\infty + \frac{u_\infty^2}{2} \tag{23}$$

$$\mathrm{P_{st}} \approx \rho_\infty^2 u_\infty^2 \tag{24}$$

It is assumed that the local enthalpy of the gas is significantly greater than the local wall enthalpy. The local wall enthalpy is therefore negligible. It is also assumed that the kinetic energy of the fluid impacting the stagnation point is assumed to be completely converted to pressure. Equations 19, 20, and 21, are rearranged to solve for the radius of the leading-edge under a set of hypersonic heat flux conditions. The leading-edge radius for the Tauber-Meneses and Sutton-Graves equations are as follows:

$$R = \left(\frac{\rho_\infty^{0.5} V_\infty^3 (1.83 \times 10^{-8} R^{-0.5})\left(1 - \frac{h_w}{h_o}\right)}{\dot{q_w}}\right)^2 \tag{25}$$

$$R_n = \left(\frac{k\sqrt{\rho}V^3}{\dot{q}_w}\right)^2 \tag{26}$$

$$R_{le} = \left(\frac{H_\infty K\sqrt{P_{st}}}{\dot{q_{cw,st}}}\right)^2 \tag{27}$$

Depending on which operating conditions are known to the user, the equations provided above produce radius values that can be inserted into Equation 14.

3.2.3 Inverse Airfoil Fitting

The CST method is used to generate a variety of geometries. The CST method can also be employed to approximate existing geometries. [34] This inverse CST method involves reading in a list of x and z – coordinates from an xlsx file. The x and z – coordinates for specific airfoils are obtained from *Airfoil Tools*. [35] The x – coordinates are used with an initial weight coefficient guess in the CST method to calculate z – coordinates. The difference between the CST approximation and original value is calculated. The least squares error is minimized using the 'Nelder-Mead' optimizer in the Python SciPy package. The 'Nelder-Mead' optimizer is selected because it only requires the objective function to be evaluated and does not need to calculate the derivatives for optimization. Additionally, it can handle several independent variables. [36] [37] The minimization stops once maximum number of iterations or tolerance of $1x10^{-4}$ has been achieved. The first optimization process results in a new set of weight coefficients for a specific airfoil geometry.

3.2.4 Aerodynamic Performance

Aerodynamic efficiency analysis is needed to understand how geometries perform once it has been altered by the effects of stagnation point heat flux. The algorithm was first built around *XFoil* which is a design and analysis tool used for airfoils under subsonic conditions. The framework is designed such that it can read in an airfoil, Reynolds number, Mach number, angle of attack, and number of iterations. The output of *XFoil* gives the lift and drag polars for the specific airfoil under the given conditions. [38] [39] The metric of interest is the lift-to-drag ratio. However, *XFoil* analysis is only valid for subsonic flow. In

order to analyse the airfoils generated under hypersonic conditions, a low-fidelity hypersonic analysis tool, *MicroCFD*, is incorporated into the algorithm. *MicroCFD*, like *XFoil*, is used to obtain the necessary lift and drag polars. However, the hypersonic analysis cannot be automated as there is no existing Python API for *MicroCFD.*

3.2.5 Aerodynamic Shape Optimization

Aerodynamic shape optimization is necessary to find the optimized airfoil after the stagnation point heat flux radius is applied. The SLSQP optimizer from the Python SciPy package is used to employed to minimize the inverse lift-to-drag ratio or maximize C_L/C_D. [40] The SLSQP optimizer is selected for the second optimization due to several constraints. [41] [42] The first constraint is keeping the first weight coefficient for the upper and lower surface constant as this is determined from the heat flux equations. The optimizer is the given bounds for the remaining coefficients, the lower bounds for the upper surface are kept to 80% of the original weight and the limit of the upper bounds is 120%. For the lower surface, the lower bound is limited to 120% and the upper bound is set to 80%. The lower surface bounds are flipped due to typically having negative values. The third constraint pertains to having an inequality constraint for the area of the airfoil. The area of the airfoil is calculated through each iteration but is constrained such that it cannot fall below 95% of the starting area. This area constrain is similar to that employed by *Straathof et al.* and *Zhu.* [25] [43] This constraint is in place as the optimizer would solve for the thinnest airfoil possible, but in reality, the airfoil has to have space for sensors and internal structure. The optimization can then be described by Equation 28:

$$\min \frac{C_D}{C_L}$$
$$\text{subject to } \mathrm{A}_0 = A_0, \mathrm{V} \geq \mathrm{V}_0 \tag{28}$$

where A_0 is the weight coefficient set by stagnation point heat flux, and V is the area of the entire airfoil.

CHAPTER 4: RESULTS AND ANALYSIS

This chapter highlights the use of importing existing airfoils, calculating new leading-edge radii, and applying the radius values to the CST method. This chapter also includes the steps taken to examine the aerodynamic performance of the heat flux generated airfoils and optimize the airfoils for maximum aerodynamic efficiency given the constraints mentioned in section 3.2.

4.1 Application of CST Method

As previously mentioned, the objective of this research is to take the CST method and integrate the parameterization with stagnation point heat flux. The CST method is benchmarked to create a series of geometries airfoils as well as importing existing airfoils. The airfoils generated herein are the: unit airfoil, NACA0012, NACA66-206, and the NSC 2-0714. Figure 12 below shows the unit airfoil when all weight coefficients are set to 1 making the shape function, $S(x) = 1$. Figure 13 shows a shape change caused by altering the exponents used with the class function. The shapes generated are verified with function parameters and geometries in research by *Kulfan.* [18] [19]

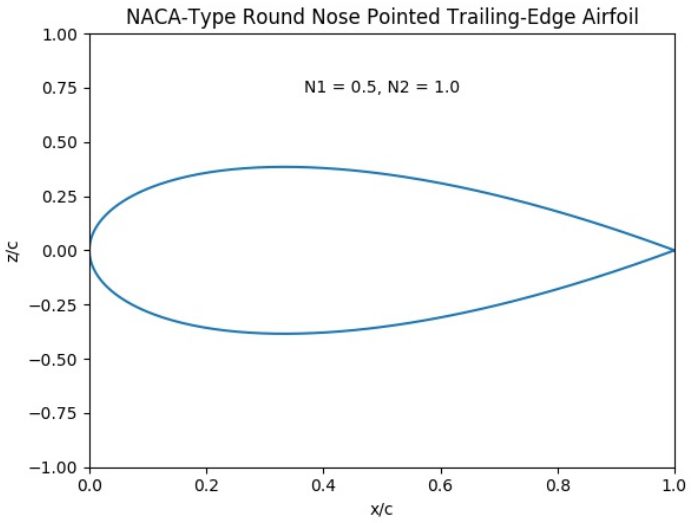

Figure 12: Round nose, pointed trailing edge unit airfoil

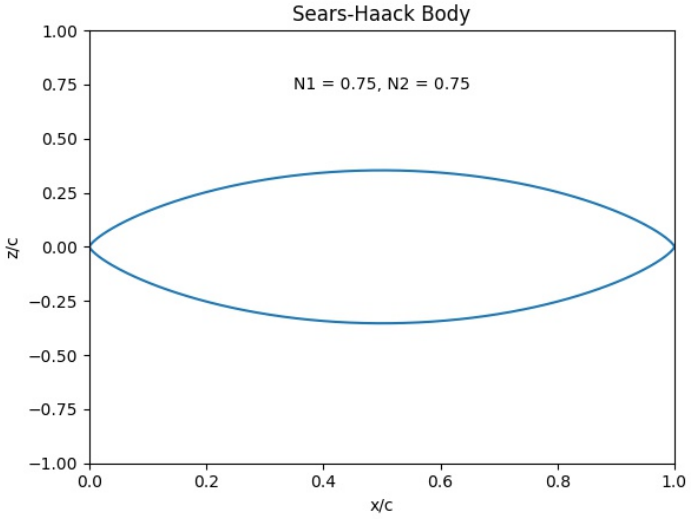

Figure 13: Sear-Haack body with N1 = 0.75 and N2 = 0.75

Additional steps to verify that the CST method is working properly involves perturbing the values of the weight coefficients.

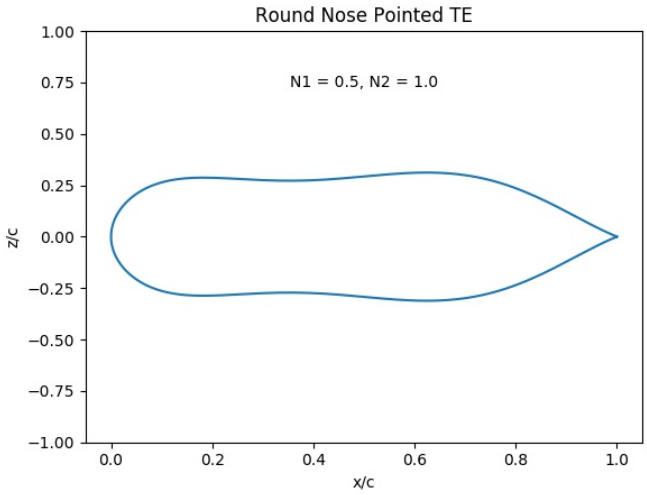

Figure 14: Round nose, pointed trailing edge geometry with mid-body adjustments

Figure 14 shows the alteration of the unit airfoil by changing the middle values of the weight coefficients. The values are set to A = [1, 1, 0.0001, 1, 1.9, 1]. The weight coefficients for the lower surface possess the same magnitude but are negative as this makes a symmetrical geometry. Figure 15 illustrates an airfoil geometry produced using unsymmetrical weights for the upper and lower surface.

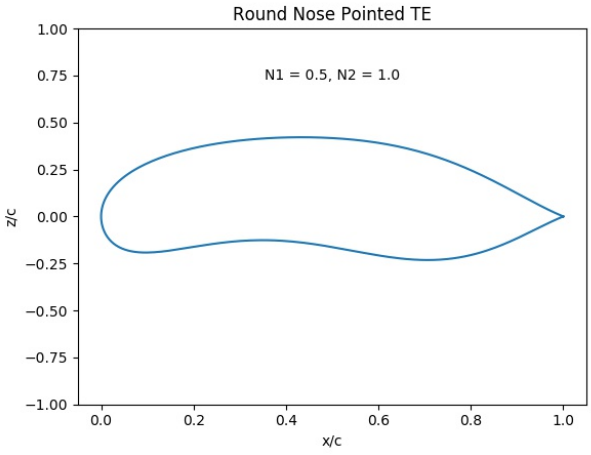

Figure 15: Airfoil geometry generated using unsymmetrical weights

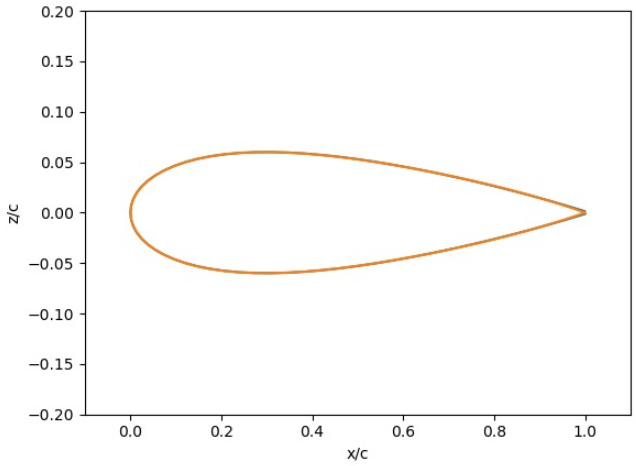

Figure 16: CST approximation of NACA0012 airfoil

Figure 16 shows the NACA0012 airfoil approximated with the CST method using 82 x-coordinate points. The approximated curve is shown with the orange superimposed on top of the original airfoil shown by the blue curve. It can be seen that the approximation of the NACA0012 airfoil is extremely accurate. Figure 17 shows the approximation of the NACA66-206 airfoil with the CST method. It can be seen that the approximated airfoil, shown again in orange, is not perfectly superimposed on the original blue curve though it is extremely close.

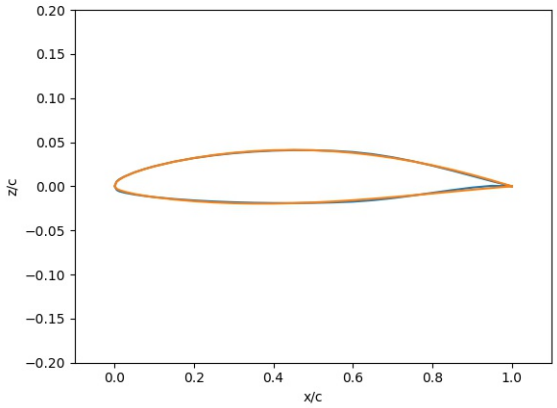

Figure 17: CST approximation of NACA66-206 airfoil

The third approximated airfoil is the NSC 2-0714 airfoil as shown in Figure 18. It can be seen that there is a slightly discrepancy at the trailing edge of the geometry. The original airfoil in blue depicted in blue does not form a closed geometry with the given coordinates. [44] The CST method is able to approximate the curve and form a closed geometry. However, the approximated curve from the CST method does not accurately approximate the curvature of the trailing edge. It can be seen that the CST method is implemented correctly and can be used to approximate the existing geometries.

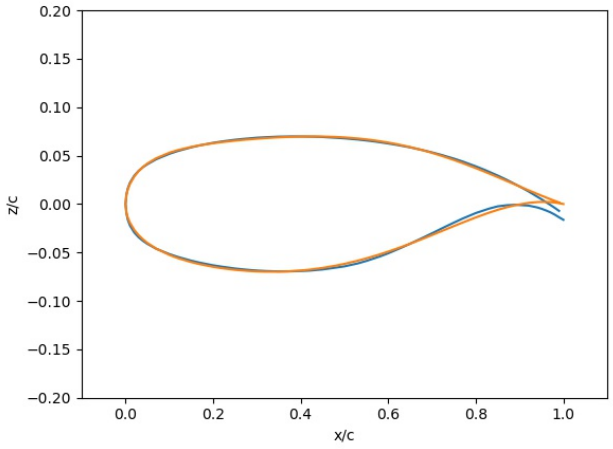

Figure 18: CST approximation of NSC 2-0714 airfoil

4.2 Stagnation Point Heat Flux

Using the equations detailed in section 3.2, several leading-edge radii are calculated with hypersonic operating conditions extracted from literature. The first test case utilized data from *Anderson* which are provided in Table 3: [1]

Table 3: Hypersonic operating parameters for the space shuttle

Density, ρ_∞ (kg/m^3)	Velocity, V_∞ (km/s)	T_w (K)	C_p (J/kg K)	$\dot{q_w}$ (W/cm^2)	R (m)
1.075E-4	219.58	1110	1004.5	45.78	1.29

The radius of the leading-edge is a given value from *Anderson* and Equation 19 was used to solve for the heat flux in W/cm^2. The chord was not given as part of the data and so the radius value of 1.29m is normalized with a chord value of 1m. Figure 19 shows the comparison of R = 1.29m in green to a unit airfoil in blue.

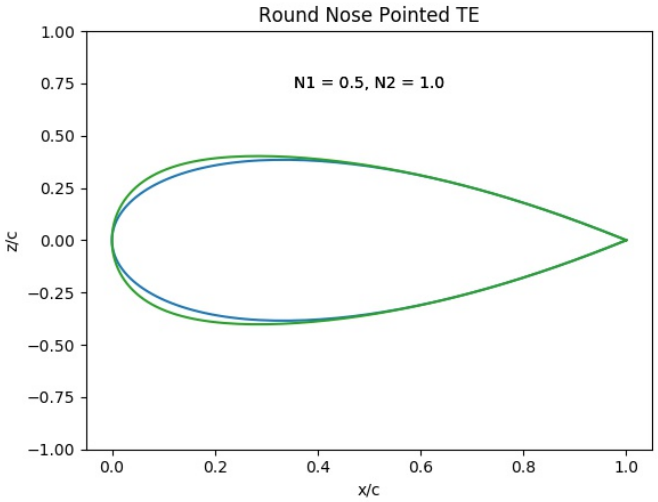

Figure 19: Leading-edge radius comparison with unit airfoil

Subsequently, it is of interest to examine radius values obtained using the *Sutton-Graves* equations. Additional parameters are required to determine the leading-edge radius using Equation 27. The parameters provided in Table 4 correspond to an altitude of 68.9 km. For the purpose of obtaining freestream temperature, the altitude is rounded up to 70 km. [26]

Table 4: Leading-edge radius using Sutton-Graves

c_p (J/kg K)	T_∞ (K)	ρ_∞ (kg/m^3)	V_∞ (km/s)	K	R (m)
1004.5	219.58	1.075E-4	6.61	3.6E-4	1.414

Another leading-edge radius value is obtained using the second *Sutton-Graves* heat flux equation. Equation 26 only needs the freestream density, flight velocity, heat flux value, and a thermal coefficient which is set to k = 1.71415E-4 for Earth's atmosphere. The parameters and resulting radius value are provided in Table 5.

Table 5: Leading-edge radius using second Sutton-Graves equation

ρ_∞ (kg/m^3)	V_∞ (km/s)	k	R (m)
1.075E-4	6.61	1.71415E-4	1.298

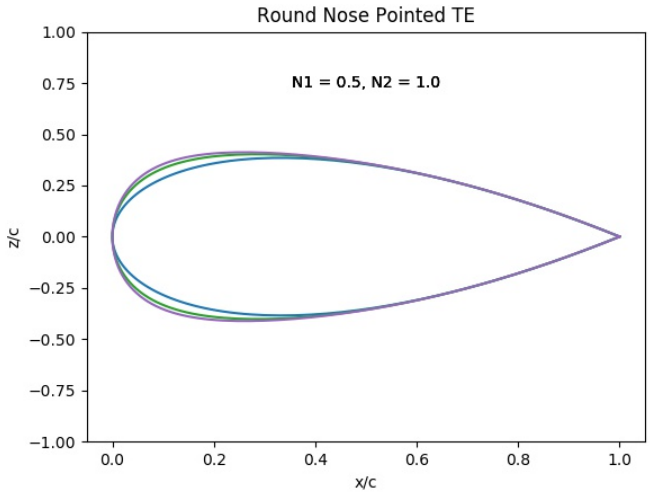

Figure 20: Comparison of radii between *Tauber-Meneses* and *Sutton-Graves* equations

Figure 20 shows the different radii determined from Table 5 conditions. The second *Sutton-Graves* equation results in a 0.62% error, likely due to the fact that it does not require the temperature assumption.

The second test case also involves hypersonic conditions applied to space shuttle research which are tabulated in Table 6: [46]

Table 6: Space shuttle operating conditions

Flight Condition	Altitude (km)	Pressure (Pa)	Temperature (K)	Velocity (m/s)	$\dot{q}$ (W/m^2)	ρ (kg/m^3)
Hypersonic	74	4	210	6700	444,011	4.637E-5

The assumptions for the proceeding values included the atmosphere being calorically perfect and a density value obtained from PDAS tables. [45] The study utilizes the NACA0012 airfoil as the baseline airfoil with the radius of curvature equal to 0.690 m. The weight coefficients are determined by first importing the NACA0012 airfoil. Knowing that at x = 0, $A_0 = \sqrt{\frac{2R_{le}}{c}}$ the chord value, *c*, is calculated. By holding the chord value as a constant value, a new A_0 can be calculated with the three heat flux equations as tabulated in Table 7. The error for the *Tauber-Meneses* equation is 12.5%, significantly larger than the error for the *Sutton-Graves* equations. The larger error can be attributed to assuming that the given stagnation temperature is equal to the wall temperature. The *Tauber-Meneses* heat flux equation is therefore more sensitive because it needs more accurate values, in this case the actual wall temperature.

Table 7: Leading-edge and first weight coefficient for all heat flux equations

Heat Flux Equation	R_{LE} (m)	A_0	Percent Error (%)
$\dot{q}_w = k\left(\frac{\rho}{R_n}\right)^{\frac{1}{2}} V^3$	0.645	0.152	6.52
$\dot{q}_{cw,st} \approx H_\infty K \sqrt{\frac{P_{st}}{R_{le}}}$	0.702	0.158	1.74
$\dot{q}_w = \rho_\infty^{0.5} V_\infty^3 (1.83 \times 10^{-8} R^{-0.5})\left(1 - \frac{h_w}{h_o}\right)$	0.604	0.147	12.5

Boost-glide vehicle operating altitudes are not as high 70 km rather in the range of 10 – 30 km. In works presented by *Kasen* and *Steeves*, a set of operating conditions in Table 8 are provided for an air-breathing hypersonic vehicle traveling Mach 6 – 8 at a dynamic pressure of 48kPa. The radii values that are extracted from these conditions are on the scale of millimeters which match the values can be seen in Figure 21. [47] Table 9 gives the leading-edge radius for three selected heat flux values at Mach 6, 7, and 8.

Table 8: Operating conditions for Mach 6, 7, and 8 at dynamic pressure of 48 kPa

Mach	Altitude (km)	Density (kg/m^3)	Velocity (km/s)	Enthalpy (MJ/kg)	Stagnation Temperature (K)	Stagnation Pressure (kPa)
6	26.93	0.0296	1.80	1.85	1651	95.90
7	28.98	0.0215	2.11	2.46	2122	95.72
8	30.76	0.0160	2.42	3.16	2627	93.70

Table 9: Leading-edge radii at 1, 2, and 6 MW/m^2

Mach	Heat Flux (MW/m^2)	Leading-Edge Radius (m)
6	1	0.043
	2	0.011
	6	0.0012
7	1	0.075
	2	0.019
	6	0.00208
8	1	0.1213
	2	0.03032
	6	0.00337

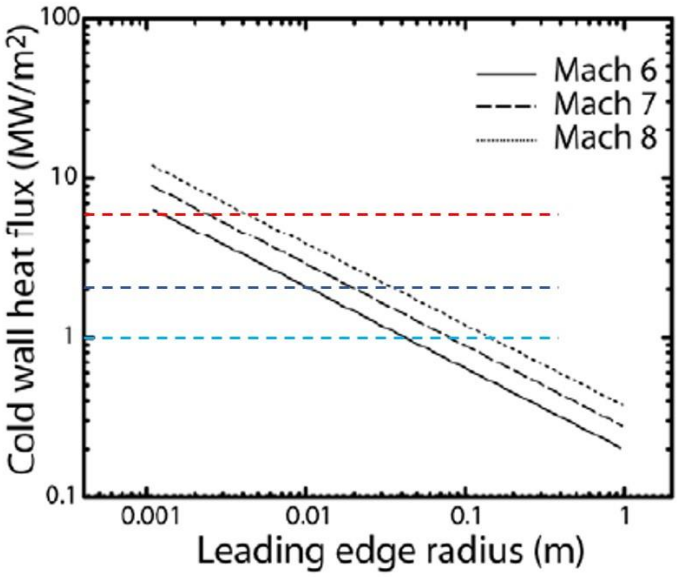

Figure 21: Cold-wall heat flux for Mach 6-8 at dynamic pressure of 48 kPa

4.3 Two-dimensional Aerodynamic Shape Optimization

The objective of this second optimization is to analyze assess the aerodynamic efficiency of the two-dimensional airfoils that have heat flux conditions applied to the leading-edge of the geometry. As mentioned before, the optimization process takes an airfoil and holds the first weight coefficient obtained from the heat flux conditions constant. The remainder of the weight coefficients are allowed to be perturbed with limits of 80% and 120% of the original coefficient. The limits pertain to the movement of z-coordinates so that the optimizer does not obtain an extremely thin airfoil. An additional inequality constraint is imposed in the optimizer such that the area of the airfoil must be greater than or equal to 90% of the original airfoil. The steps taken to obtain aerodynamically optimized airfoils are as follows:

1. Import airfoil coordinates list using "pandas.read_excel" function [48]
2. Optimize initial weight coefficients
3. Calculate leading-edge from heat flux conditions
4. Replace first upper and lower weight coefficient with new leading-edge radii value
5. Run CST method to obtain new geometry, calculate new area
6. Output geometry to .shp file
7. Adjust tunnel settings in *MicroCFD*, import airfoil geometry [49]
8. Run test to obtain C_L and C_D
9. Input C_L and C_D into optimizer to obtain new weight coefficients
10. Repeat steps 5 – 9

Once the optimizer exits, the output will contain an optimized lift-to-drag ratio as well as a new area for the airfoil geometry.

4.3.1 MicroCFD Wind Tunnel Settings

The leading-edge radius values that are calculated in section 4.2 are assumed to be applied airfoils with a chord value of 1m. As such, the wind tunnel in *MicroCFD* is adjusted to analyse airfoils that are 1m in length. The wind tunnel length is then set to be 4m as recommended by user documentation. [49] The flow Mach number is set to Mach 6, and the pressure and temperature are set to 16 hPa and 224.5 K which are values obtained from PDAS, assuming an altitude of 28 km. [45] The angle of attack for the experiments is set to 2°.

4.4 Experiments

The NSC 2-0714 supercritical airfoil, NACA 0012-64, and NACA 66-206 are selected as the test airfoils for heat flux application. The heat flux conditions from the research done by *Steeves et al* are applied using Equation 27. The initial weight coefficients that are supplied to the optimizer are:

$$A = [\,1 \quad 1 \quad 1 \quad -1 \quad -1 \quad -1] \tag{29}$$

After the initial optimization, the weight coefficients become:

$$A = [0.18572 \quad 0.16598 \quad 0.24203 \quad -0.16544 \quad -0.25936 \quad 0.00663] \tag{30}$$

The Mach 6 with heat flux of 6×10^6 MW/m^2 conditions from Table 8 are applied and the radius value is then used in Equation 14 to determine the weight coefficient values assuming a chord value of 1. Equation 30 then becomes the following:

$$A = [0.04861 \quad 0.16598 \quad 0.24203 \quad -0.04861 \quad -0.25936 \quad 0.00663] \quad (31)$$

Figure 22 shows the lift-to-drag ratio history through the iterations with a mean of 1.6235 through 56 iterations. The optimization showed no variation after 48 iterations. The lift-to-drag ratio between the initial application of heat flux and aerodynamic optimization increased by 4.3% while the area of the airfoil increased by less than 1% as show in Table 10. After iterating through the SLSQP optimizer, the resulting aerodynamically optimized airfoil is shown in Figure 23. The final weights after the optimization are as follows:

$$A = [0.04861 \quad 0.14938 \quad 0.26623 \quad -0.04861 \quad -0.26695 \quad 0.00597] \quad (32)$$

A comparison of the coefficients in Equation 31 and Equation 32 shows that the first weight coefficient was kept the same throughout the optimization process, thereby keeping the leading-edge geometry constant.

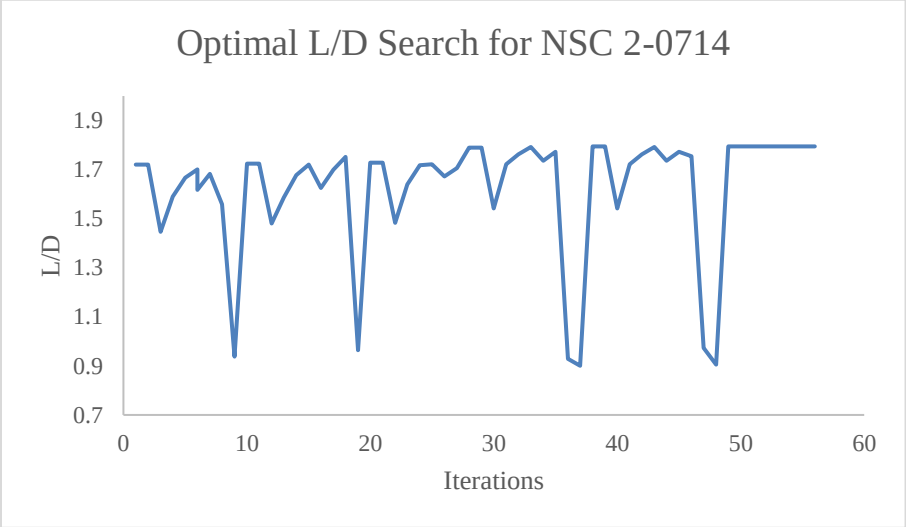

Figure 22: Optimal L/D iterative search for NSC 2-01714

Table 10: Change in lift-to-drag and area after optimization for NSC 2-0174

$L/D_{initial}$	L/D_{final}	Percent Change (%)	Initial Area	Final Area	Percent Change (%)
1.7207	1.7946	4.3	0.06799	0.06865	0.97

Given that the airfoils are under hypersonic flow conditions, a small 4.3% increase in lift-to-drag can be extremely valuable.

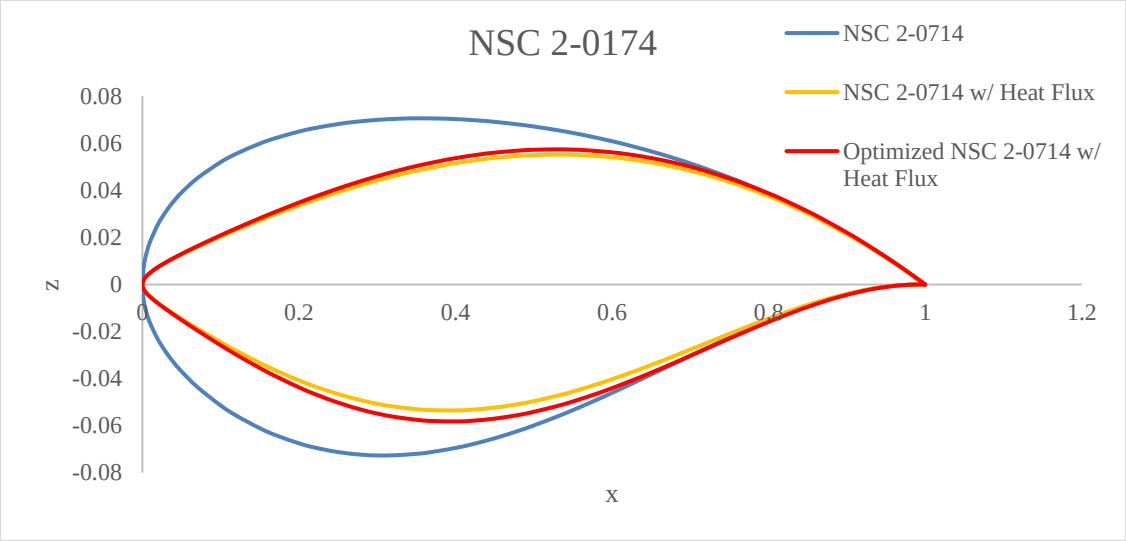

Figure 23: Aerodynamic shape optimization of NSC 2-0714 airfoil

The Mach number variation shown in Figure 24 indicates the Mach number is lowest at the leading-edge.

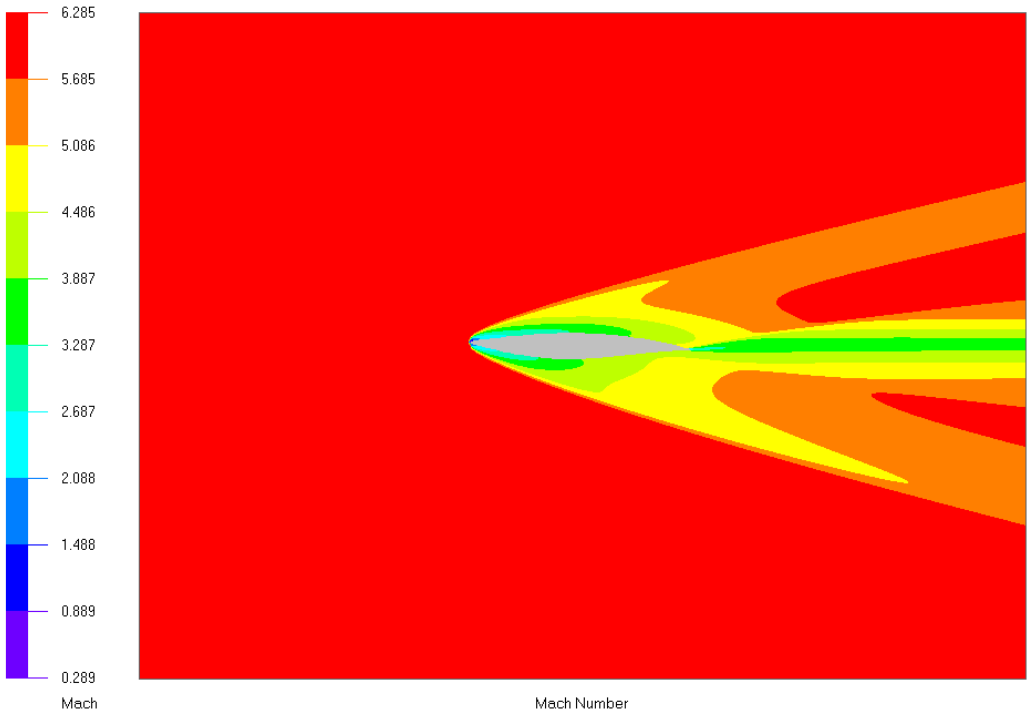

Figure 24: Mach number variation for the optimized NSC 2-0174 airfoil with heat flux

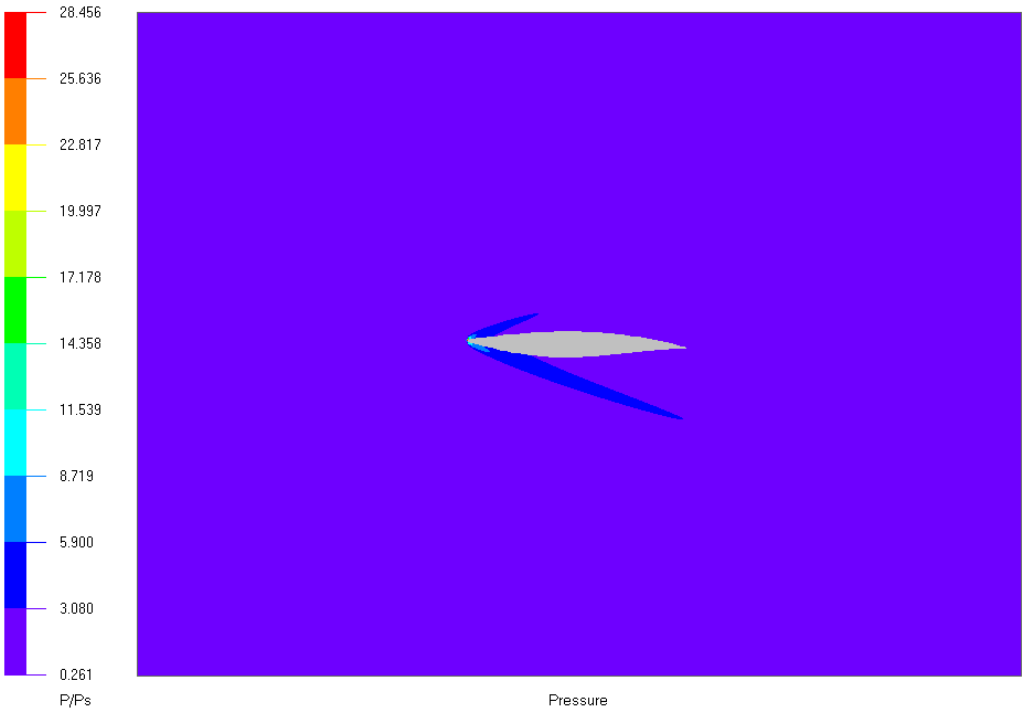

Figure 25: Pressure variation for the optimized NSC 2-0174 airfoil with heat flux

Figure 25 and Figure 26 show the pressure and temperature variation over the NSC 2-0714 under the Mach 6 flow conditions.

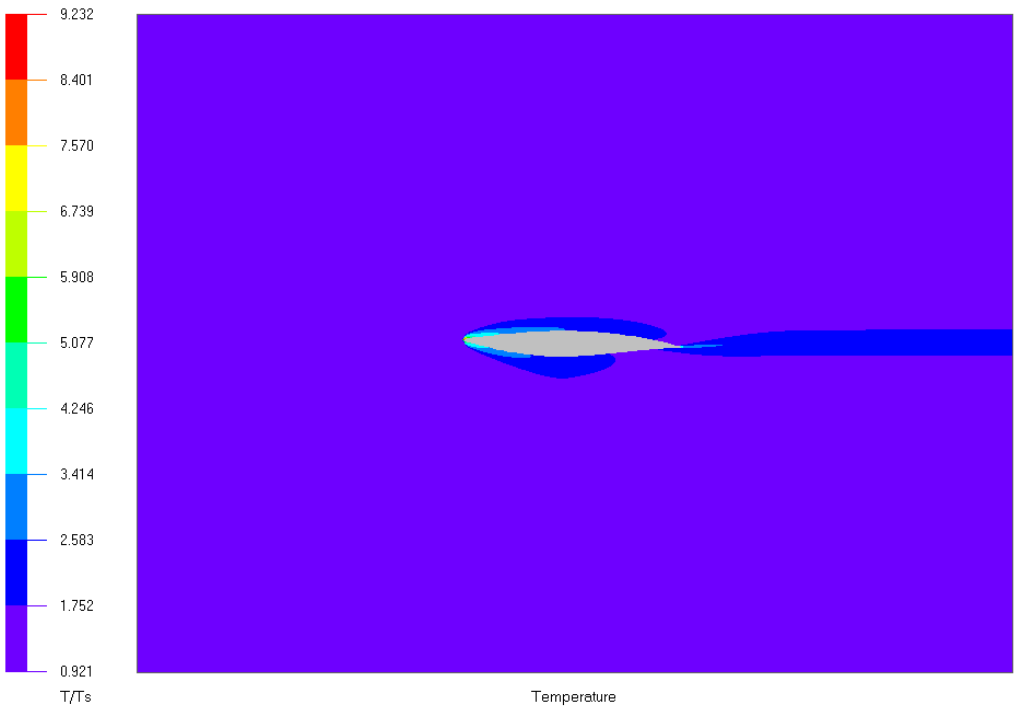

Figure 26: Temperature variation for the optimized NSC 2-0714 airfoil with heat flux

The Mach 6 conditions and a heat flux value of $6x10^6$ W/m^2 are applied to the NACA 0012-64 airfoil. Equation 33 are the weight coefficients for the NACA 0012-64 airfoil. The conditions in *MicroCFD* are set to be identical with the conditions as the NSC 2-0174. After 19 iterations through the optimizer, it is found that the optimal airfoil is the same as the initial airfoil. Following the optimization history shown in Figure 27, the optimal airfoil was found after the 12th iteration. The lift-to-drag ratio and areas for initial and optimized are tabulated in Table 11 which also shows there was no change in the airfoil shape. Figure 28 shows the shape of the original NACA 0012-64 along with the airfoil with the leading-edge radius obtained the heat flux.

$$A = [0.04861 \quad 0.14120 \quad 0.21613 \quad -0.04861 \quad -0.14120 \quad -0.21608] \quad (33)$$

Table 11: Change in lift-to-drag and area after optimization for NACA 0012-64

$L/D_{initial}$	L/D_{final}	Percent Change (%)	Initial Area	Final Area	Percent Change (%)
1.4587	1.4587	0	0.065501	0.065501	0

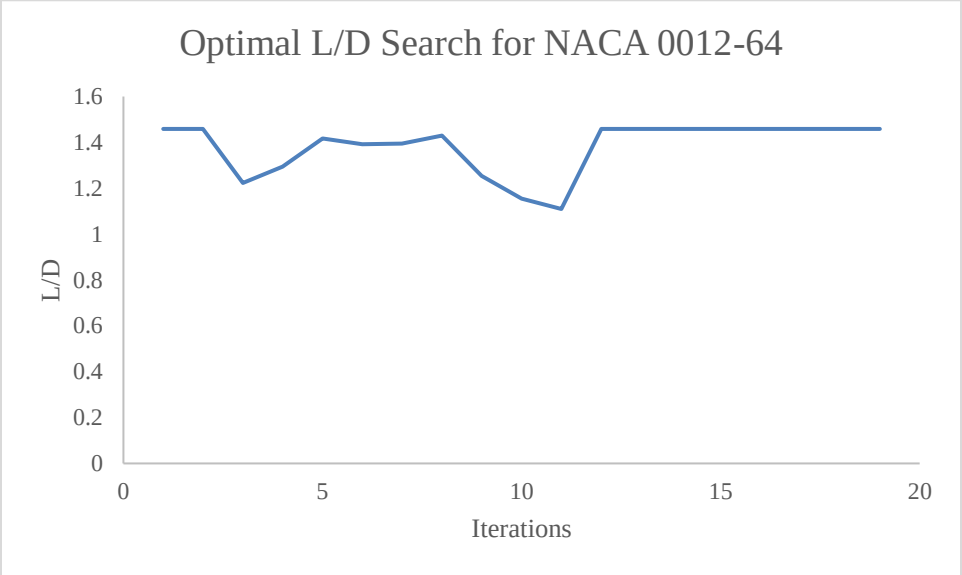

Figure 27: Optimal L/D iterative search for NACA 0012-64 airfoil

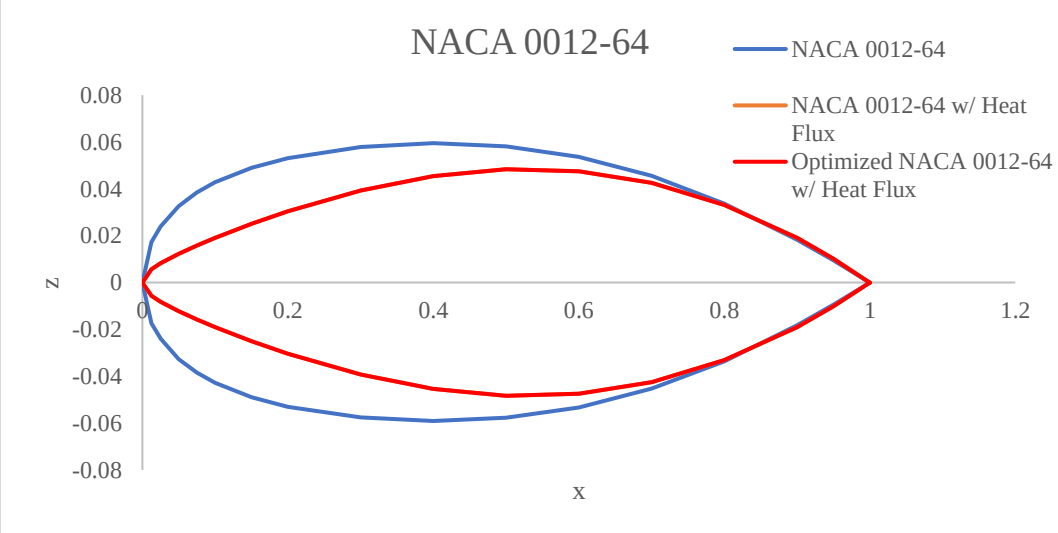

Figure 28: Aerodynamic shape optimization of NACA 0012-64 airfoil

In Figure 29, it can be observed that the Mach number at the leading-edge is low, as expected due to it being at the stagnation point of the airfoil.

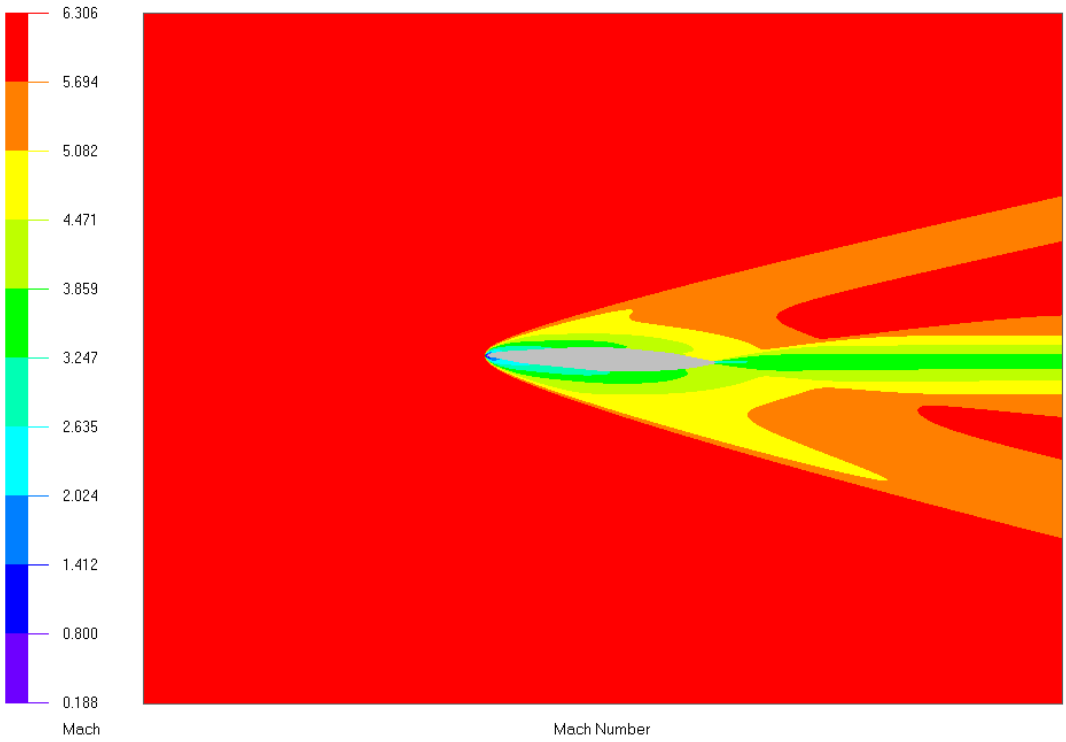

Figure 29: Mach number variation for the optimized NACA 0012-64 airfoil with heat flux

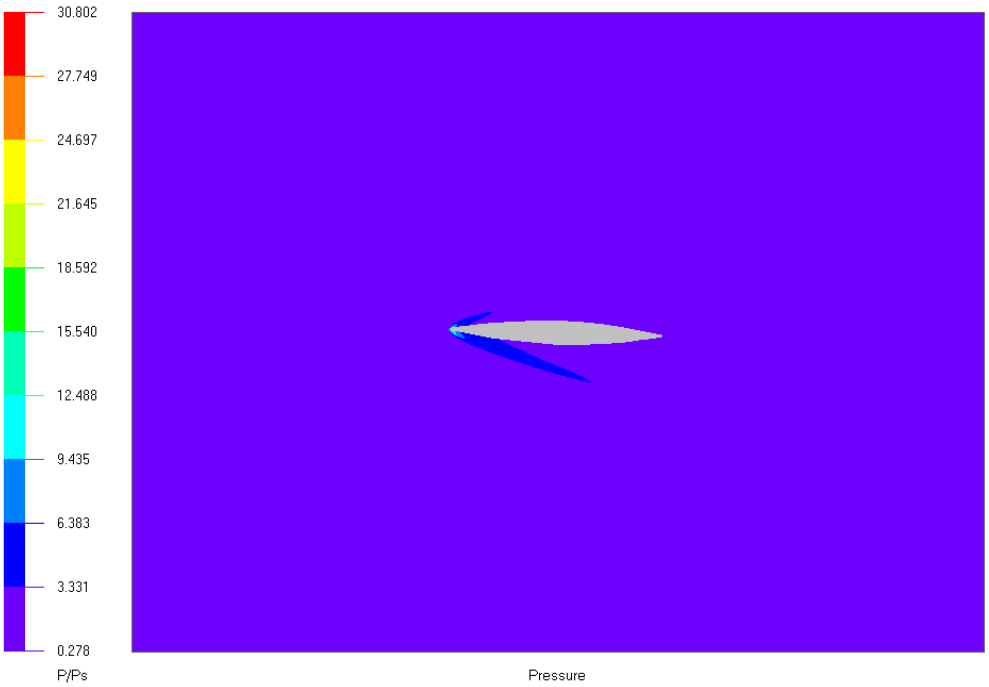

Figure 30: Pressure variation for the optimized NACA 0012-64 airfoil with heat flux

The pressure distribution over the airfoil is shown in Figure 30. It can be seen that the maximum pressure occurs at leading-edge of the airfoil. Similarly, Figure 31 shows the temperature distribution over the airfoil where the maximum temperature for the airfoil occurs at the stagnation point of the leading-edge.

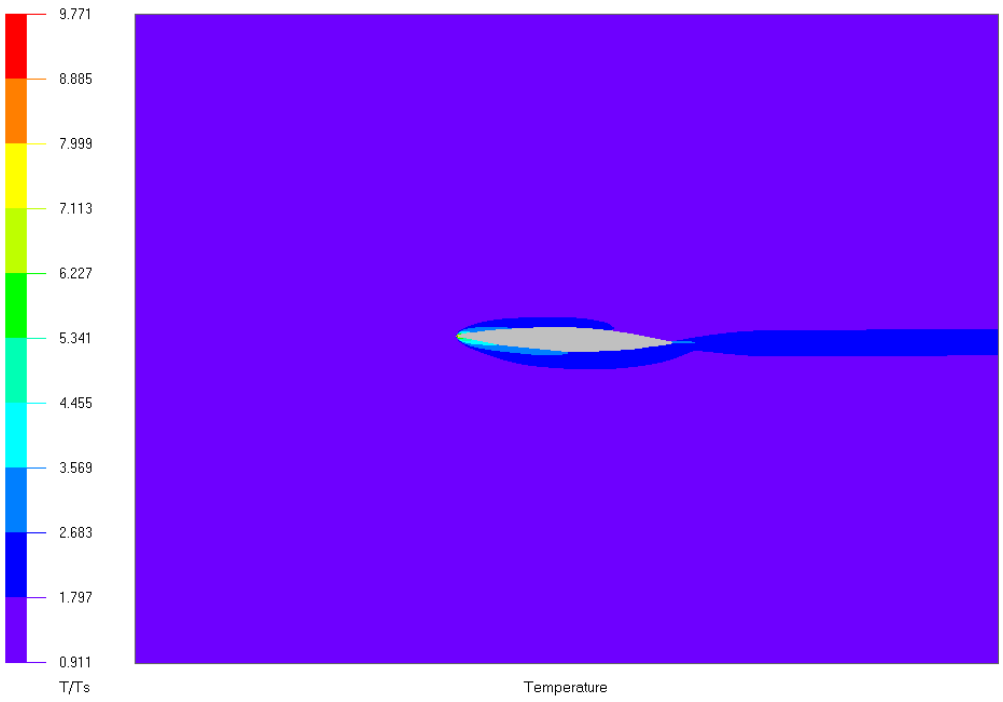

Figure 31: Temperature variation for the optimized NACA 0012-64 airfoil with heat flux

Equation 34 provides the initial weight coefficients that fit the NACA 66-206 airfoil. The first coefficient on the for the upper and lower surfaces are the same values as the NSC 2-0714 and NACA 66-206 airfoils as they are subject to the same heat flux conditions.

$$A = [0.04861 \quad 0.12666 \quad 0.14080 \quad -0.04861 \quad -0.06688 \quad -0.03554] \quad (34)$$

The optimization history for the NACA 66-206 airfoil is shown in Figure 32. The optimization for the NACA 66-206 finished in 26 iterations, almost half that of the NSC 2-0714. This can be attributed to the thickness of the airfoils where the initial NACA 66-206 is already less than the initial thickness of the NSC 2-0174.

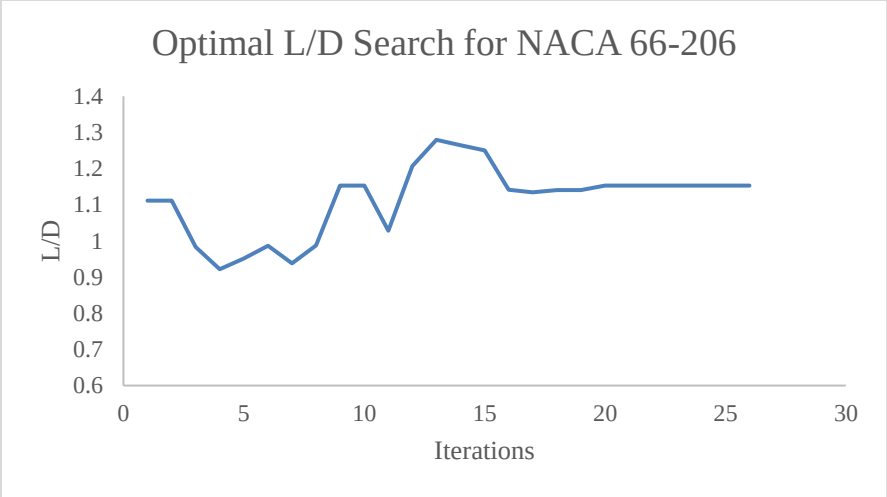

Figure 32: Optimal L/D iterative search for NACA 66-206 airfoil

Equation 35 gives the new weight coefficients after optimizations of the NACA 66-206 airfoil. Once again, the first and lower surface weight coefficients are kept constant to maintain the same leading-edge radius.

$$A = [0.04861 \quad 0.12033 \quad 0.13376 \quad -0.04861 \quad -0.07022 \quad -0.03732] \quad (35)$$

Table 12: Change in lift-to-drag and area after optimization for NACA 66-206

$L/D_{initial}$	L/D_{final}	Percent Change (%)	Initial Area	Final Area	Percent Change (%)
1.112	1.153	3.69	0.040645	0.040009	1.57

After the 26 iterations through the optimization process, the lift-to-drag ratio was increased by 3.7% and area was decreased by 1.57% as tabulated in Table 12. The area within the airfoil changed minimally, resulting in the airfoil shown in Figure 33.

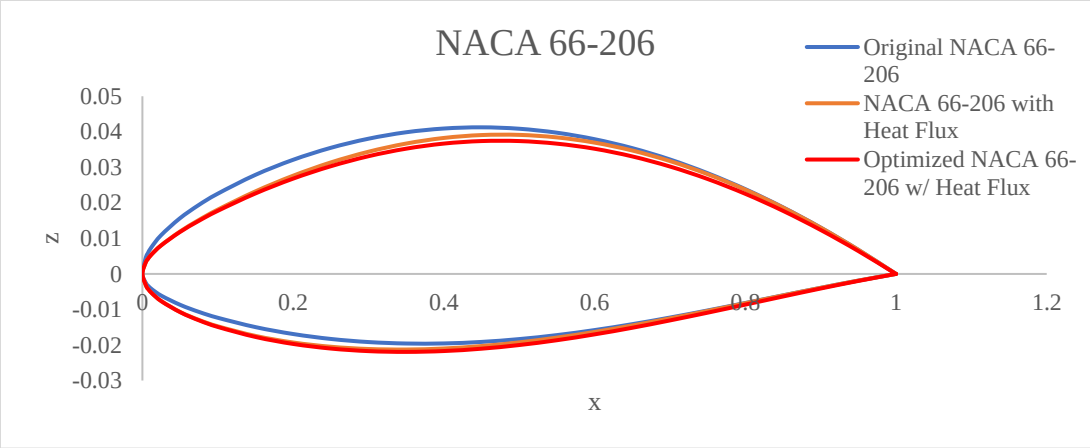

Figure 33: Aerodynamic shape optimization of NACA 66-206 airfoil

It is observed that there is only a slight change in the airfoil geometry that results in a 3.7% increase in lift-to-drag ratio. The Mach, pressure, and temperature variation for the NACA 66-206 airfoil are shown in Figure 34, Figure 35, Figure 36, respectively.

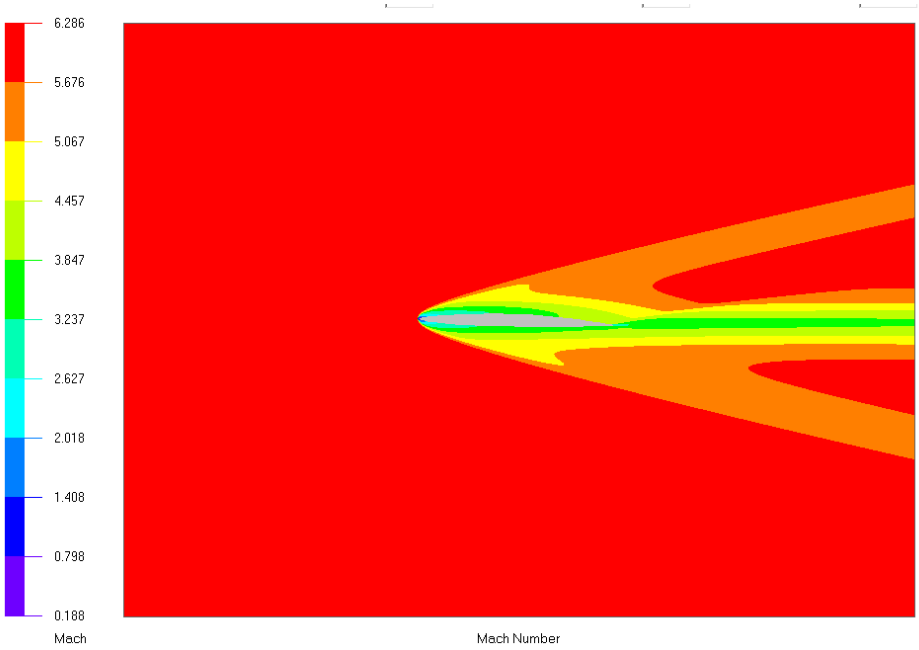

Figure 34: Mach number variation for the optimized NACA 66-206 airfoil with heat flux

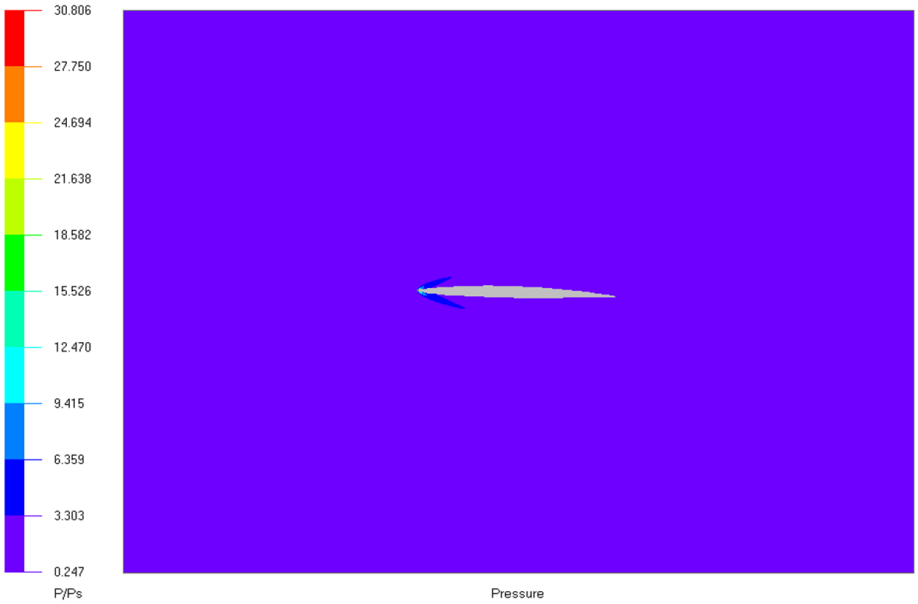

Figure 35: Pressure variation for the optimized NACA 66-206 airfoil with heat flux

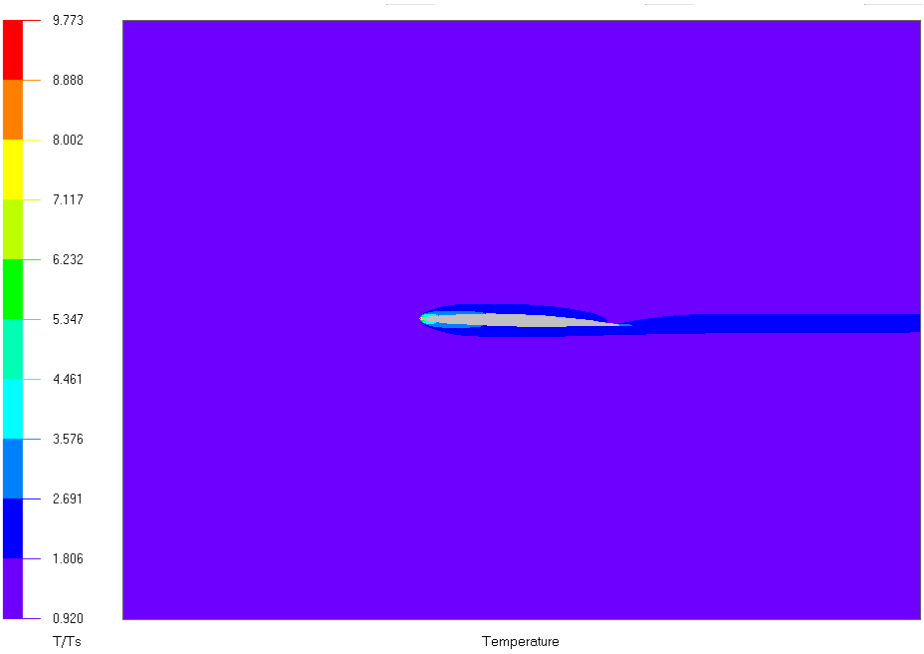

Figure 36: Temperature variation for the optimized NACA 66-206 airfoil with heat flux

It is important to note here that the NACA 66-206 is the most relevant airfoil of the three selected to the hypersonic regime. This is because it is designed to be a supersonic airfoil. [50]

4.5 Summary

Table 13 provides a summary of the lift-to-drag ratios and areas of the selected airfoils. It can be seen that the aerodynamic efficiency for two of the selected airfoils are increased through the optimization process. The maximum temperature for the NSC 2-0174 airfoil is 2,073K and 2,194K for the NACA 0012-64 and NACA 66-206 airfoils at the leading-edge, as determined by *MicroCFD*.

Table 13: Aerodynamic efficiency and area evaluation for airfoils linked with heat flux

Airfoil	Initial L/D	Optimized L/D	Percent Change (%)	Initial Area	Optimized Area	Percent Change (%)
NSC 2-0174	1.7207	1.7946	4.3	0.06799	0.06865	0.97
NACA 0012-64	1.4587	1.4587	0	0.065501	0.065501	0
NACA 66-206	1.112	1.153	3.69	0.040645	0.040009	1.57

CHAPTER 5: CONCLUSION AND FUTURE WORK

5.1 Review of Research Questions and Hypotheses

The literature review revealed an important gap previously mentioned in section 2.3 which led to the formulations of several research questions and hypotheses. This section focuses on re-addressing the research questions and the associated hypotheses using the results obtained from the previous chapter.

Research Question #1: *How can aerodynamic heating be incorporated into CST hypersonic parameterization?*

5.1.1 Research Question 1

The hypothesis connected with Research Question 1 is:

Hypothesis 1: *If the leading-edge from stagnation point heat flux is linked with the first weight coefficient in the CST method, then aerodynamic heating can be incorporated into CST shape parameterization.*

Hypothesis 1

There is very tight coupling between disciplines for the hypersonic design process. While the CST method has been utilized to produce hypersonic geometries, which are then optimized for aerodynamic efficiency. A major gap in CST hypersonic design is the inclusion of aerodynamic heating as a constraint. The CST method enables direct control over specific parameters such as the leading-edge radius and boat-tail angle and thickness.

The shape of the leading-edge radius is a critical variable in stagnation point heat flux. Leveraging the CST method led to the ability to generate geometries with leading-edge shapes specific to desired or allowable heat flux. Thus, hypothesis 1 is validated through connecting the leading-edge radius from stagnation point heat flux formulas to the weight coefficient in the CST method

Research Question 2: *How will aerodynamic efficiency for 2D airfoils change with heat transfer rates and area constraints?*

The aerodynamic efficiency of aircraft is often measured by the lift-to-drag ratio. Thinner objects typically experience lower drag which results in higher aerodynamic efficiency. However, due to area or volume constraints as well as having specific leading-edge geometry, reducing airfoils down to extremely thin shapes is no longer feasible. After producing geometries that hold the leading-edge radius constant, it is shown that the optimization process is able to increase the aerodynamic efficiency by a small percentage while still staying within the limits of the area.

5.2 Summary

The primary research objective in this thesis was to enhance the CST method.in its use as parameterization of hypersonic shape design. This was done by incorporating the effects of aerodynamic heating, specifically stagnation point heat flux, into the shape design process.

The first part of this thesis consisted of examining methods used to parameterize hypersonic geometries. The CST method was selected as the parameterization method as

it allows for flexible control over the geometry. It is also mathematically well-behaved when designing geometries with high curvature and pointed regions. The CST method also allows for representation of geometries using a low number of design variables with inexpensive computational time. The second part of the thesis involved investigating the effects of aerodynamic heating on the leading-edge of a surface. Stagnation point heat flux equations have been developed and the heat flux experienced by a surface was found to be inversely proportional to the square root of the leading-edge radius. This was then coupled with a special characteristic of the CST method where S(0) is directly related to shaping the leading-edge radius. This allowed for the creation of unique geometries from specific heat flux conditions. Existing airfoils were parameterized with the CST method and then the leading-edge geometry was subjected to the heat flux conditions which resulted in a modified airfoil. The modified leading-edge resulted in altered aerodynamic efficiency. Therefore, like other research that have utilized the CST method, an SLSQP optimization algorithm was implemented in order to find optimal aerodynamic efficiency. The optimization was constrained by having to keep the heat flux derived leading-edge in place as well as limiting the change in area of the two-dimensional airfoils. Using a low-fidelity CFD tool, the lift and drag coefficients were input as the objective function in order to minimize the inverse lift-to-drag or C_D/C_L. The optimization process was able to produce a second modified airfoil where the lift-to-drag ratio was increased. This then resulted in a new method of implementing the CST method to design for hypersonic geometries; the leading-edge of airfoils could be controlled by desired heat flux values and the resulting airfoils could subsequently also be optimized for aerodynamic efficiency.

5.3 Future Work

5.3.1 Implement Heat Flux with Three-Dimensional CST

In previous research, it has been shown that the CST method can be extended to produce three-dimensional shapes. The stagnation point heat flux may not be constant throughout the entirety of vehicle. Hypersonic geometries and vehicles have been created using the CST method, and so it would be beneficial to include the effects of aerodynamic heating in generating three-dimensional shapes and hypersonic vehicles.

5.3.2 Aerodynamic heating on the entire geometry surface

Hypersonic flight makes for a more complex and increased difficulty in flow analysis. While aerodynamic heating at the stagnation point is the most extreme, the rest of the geometry or vehicle will also experience aerodynamic heating which can impact thermal protection systems (TPS) or cooling capabilities. Therefore, the tools that are integrated with the CST method to study hypersonics will need need to be medium – high fidelity to obtain more accurate models.

5.3.3 Complete hypersonic design

As stated previously, hypersonics is an extremely complex design process. The vehicle design will need to be optimized in all applicable disciplines, not just aerodynamic efficiency. The CST method allows for parametric shape design and it can be used to map critical parameters from different disciplines to specific components of the geometries. The connection of all relevant design disciplines to a parametric vehicle will allow for larger design space exploration in a multidisciplinary design and analysis framework.

REFERENCES

[1] H. Nishikawa, "Introduction to Waveriders," 1995. [Online]. Available: ossanworld.com/cfdnotes/cfdnotes_waverider1995.pdf. [Accessed 2019].

[2] T.-t. Zhang, Z.-g. Wang and L. Yan, "Parameterization and optimization of hypersonic-gliding vehicle configurations during conceptual design," *Aerospace Science and Technology,* vol. 58, pp. 225-234, 2016.

[3] H. J. Allen and A. Egger Jr., "A Study of the Motion and Aerodynamic Heating of Ballistic Missiles Entering the Earth's Atmosphere at High Supersonic Speeds," Ames Aeronautical Laboratory, Moffett Field, 1958.

[4] W. H. Mason, "AOE Configuration Aerodynamics," [Online]. Available: http://www.dept.aoe.vt.edu/~mason/Mason_f/ConfigAero.html. [Accessed 2019].

[5] W. F. Santos, "Simulation of Blunt Leading Edge Aerothermodynamics in Rarefied Hypersonic Flow," *Journal of the Brazilian Society of Mechanical Sciences and Engineering,* vol. 29, no. 2, pp. 123-135, 2007.

[6] J. D. Anderson , Fundamentals of Aerodynamics, New York: McGraw-Hill Education, 2017.

[7] NASA, "Entry, Splashdown, and Recovery," [Online]. Available: https://history.nasa.gov/SP-4029/Apollo_18-40_Entry_Splashdown_and_Recovery.htm. [Accessed October 2018].

[8] R. Pickrell, "The US Air Force is ordering more hypersonic weapons just one week after China tested one of its own," 2018. [Online]. Available: https://www.businessinsider.com/us-air-force-orders-hypersonic-weapons-to-compete-with-china-russia-2018-8.

[9] A. Mehta, "DefenseNews," 18 April 2018. [Online]. Available: https://www.defensenews.com/air/2018/04/18/air-force-taps-lockheed-for-new-hypersonic-cruise-missile/.

[10] NASA, "Columbia Accident Investigation Board," 2008. [Online]. Available: http://s3.amazonaws.com/akamai.netstorage/anon.nasa-global/CAIB/CAIB_lowres_full.pdf .

[11] T. A. Barber, "A Survey of Gaps, Obstacles, and Technical Challenges for Hypersonic Applications," University of Tennessee, Knoxville, 2012.

[12] Y. Jiang, C. Jiang and C.-H. Lee, "Hypersonic Aeroheating Characteristics of Leading Edges with Different Nose Radii," *Journal of Thermophysics and Heat Transfer,* vol. 31, no. 3, pp. 538-548, 2017.

[13] H. Sobieczky, "Aerodynamic Design and Optimization Tools Accelerated by Parametric Geometry Preprocessing," in *European Congress on Computational Methods in Applied Sciences and Engineering, ECCOMAS*, Barcelona, 2000.

[14] H. Sobieczky, F. C. Dougherty and K. Jones, "Hyerpsonic Waverider Design from Given Shock Waves," in *First International Waverider Symposium*, College Park, 1990.

[15] K. Kontogiannis, N. Taylor and A. Sobester, "Parametric Geometry Models for Hypersonic Aircraft: Integrated External Inlet Compression," in *54th AIAA Aerospace Sciences Meeting*, San Diego, 2016.

[16] M. A. Lobbia, "Multidisciplinary Design Optimization of Waverider-Derived Crew Reentry Vehicles," *Journal of Spacecraft and Rockets,* vol. 54, no. 1, pp. 233-245, 2017.

[17] K. G. Bowcutt, J. D. Anderson and D. Capriotti, "Viscous Optimized Hyerpsonic Waveriders," in *AIAA 25th Aerospace Sciences Meeting*, Reno, 1987.

[18] B. M. Kulfan, "Universal Parametric Geometry Representation Method," *Journal of Aircraft,* vol. 45, no. 1, pp. 142-158, 2008.

[19] B. M. Kulfan and J. E. Bussoletti, ""Fundamental" Parametric Geometry Representations for Aircraft Component Shapes," in *11th AIAA/ISSMI Mulidisciplinary Analysis and Optimization Conference*, Portsmouth, 2006.

[20] A. Mousavi, P. Castonguay and S. K. Nadarajah, "Survey of Shape Parameterization Techniques And Its Effect on Three-Dimensional Aerodynamic Shape Optimization," in *18th AIAA Computation Fluid Dynamics Conference*, Miami, 2007.

[21] S. Hua, G. Liangxian and G. Chunlin, "Research on Geometry Modeling Method Based on Three-Dimensional CST Parameterization Technology," in *16th AIAA/IISM Multidisciplinary Analysis and Optimization Conference*, Dallas, 2015.

[22] M. J. Grant and R. D. Braun, "Analytic Hypersonic Aerodynamics for Conceptual Design of Entry Vehicles," in *48th AIAA Aerospace Sciences Meeting Including the New Horizons Forum and Aerospace Exposition*, Orlando, 2010.

[23] E. D. Olson, "Three-Dimensional Piecewise-Continuous Class-Shape Transformation," in *16th AIAA/ISMO Multidisciplinary Analysis and Optimization Conference*, Dallas, 2015.

[24] M. H. Straathof, M. J. van Tooren and M. Voskuijl, "Aerodynamic Shape Parameterisation and Optimisation of Novel Configurations," in *Proceeding of the RAeS Aerodynamic Shape Parameterisation and Optimisation of Novel Configurations Conference*, London, 2008.

[25] F. Zhu, "Geometric Parameterisation and Aerodynamic Shape Optimisation," University of Sheffield, 2014.

[26] J. A. Fay and F. R. Riddell, "Theory of Stagnation Point Heat Transfer in Dissociated Air," *Journal of the Aeronautical Sciences*, vol. 25, no. 2, pp. 73-85, 1958.

[27] M. Wright and J. Dec, "Aerothermodynamic and Thermal Protect System Aspects of Entry System Design Course," 13-17 August 2012. [Online]. Available: https://tfaws.nasa.gov/TFAWS12/Proceedings/Aerothermodynamics%20Course.pdf. [Accessed November 2018].

[28] N. H. Kemp and F. R. Riddell, "Heat Transfer to Satellite Vehicles Re-entering the Atmosphere," *Journal of Jet Propulsion*, vol. 27, no. 2, pp. 132-137, 1957.

[29] G. Zuppardi and A. Esposito, "Recasting the Fay-Riddll formulae for computing the stagnation point heat flux," Universita degli Studi di Napoli 'Federico II', Naples, 2000.

[30] K. Rakesh and C. Sultan, "Parametric Geometry Model for Design Studies of Tailless Supersonic Aircraft," *Journal of Aircraft*, vol. 51, no. 5, pp. 1455-1466, 2014.

[31] M. E. Tauber, G. P. Menees and H. G. Adelman, "Aerothermodynamic of Transatmospheric Vehicles," in *AIAA and ASME, Joint Thermophysics and Heat Transfer Conference*, Boston, 1986.

[32] M. P. Loomis and G. A. Allen, Jr., "Demonstration of Integrated Trajectory/Aerothermal/TPS Sizing Design Tools for Mars Smart Lander," in *AIAA Atmospheric Flight Mechanics Conference and Exhibit*, Monterey, 2202.

[33] C. A. Steeves, M. Y. He, S. D. Kasen, L. Valdevit, H. N. Wadley and A. G. Evans, "Feasibility of Metallic Structural Heat Pipes as Sharp Leading Edges for Hypersonic Vehicles," *Journal of Applied Mechanics*, vol. 76, 2009.

[34] X. Liu and W. He, "Airfoil Optimization Design Based on the Pivot Element Weighting Iterative Method," *Multidisiplinary Digital Publishing Institute Algorithms*, pp. 1-21, 2018.

[35] "Airfoil Tools," [Online]. Available: http://airfoiltools.com/search/index. [Accessed 2019].

[36] K. Bowcutt, "Hypersonic Aircraft Optimization Including Aerodynamic, Propulsion, and Trim Effects," in *4th Symposium on Multidisciplinary Analysis and Optimization*, Cleveland, 1992.

[37] SciPy Reference Guide, "Minimize(method = 'Nelder-Mead')," [Online]. Available: https://docs.scipy.org/doc/scipy/reference/generated/scipy.optimize.minimize.html. [Accessed 2019].

[38] M. Drela, "XFoil 6.9 General Description," 30 November 2001. [Online]. Available: https://web.mit.edu/drela/Public/web/xfoil/xfoil_doc.txt. [Accessed 2019].

[39] E. Orman and G. Durmus, "Comparison of Shape Optimization Techniques Coupled with Genetic Algorithm for a Wind Turbine Airfoil," in *2016 IEEE Aerospace Conference*, Big Sky, 2016.

[40] P. Hewitt and S. Marques, "Aerofoil Optimisation Using CST Parameterisation in SU2," in *Royal Aeronautical Society Biennial Applied Aerodynamics Research Conference*, Bristol, 2014.

[41] SciPy Reference Guide, "Minimize(method = 'SLSQP')," [Online]. Available: https://docs.scipy.org/doc/scipy/reference/optimize.minimize-slsqp.html#optimize-minimize-slsqp. [Accessed 2019].

[42] Tutorials Point, "SciPy - Optimize," [Online]. Available: https://www.tutorialspoint.com/scipy/scipy_optimize.htm. [Accessed 2019].

[43] M. H. Straathof and M. J. van Tooren, "Extension to the Class-Shape-Transformation Method Based on B-Splines," *AIAA Journal*, vol. 49, no. 4, pp. 780-790, 2011.

[44] Airfoil Tools, "NASA SC(2)-0714 Airfoil," [Online]. Available: http://airfoiltools.com/airfoil/details?airfoil=sc20714-il. [Accessed 2019].

[45] R. Carmichael, "A Sample Atmosphere Table (SI Units)," Public Domain Aeronautical Software (PDAS), [Online]. Available: http://www.pdas.com/atmosTable1SI.html. [Accessed 2019].

[46] C. Zhou, Z. Wang, J. Zhi and A. Kretov, "Aerothermodynamic Optimization of Aerospace Plane Airfoil Leading Edge," *Journal of Aerospace Technology and Management*, vol. 9, no. 4, pp. 503-509, 2017.

[47] S. D. Kasen, D. T. Queheillalt, C. A. Steeves, A. G. Evans and H. N. Wadley, "A Heat Plate Leading Edge for Hypersonic Vehicles," in *ASME International Mechanical Engineering Congrass and Exposition*, Boston, 2008.

[48] DataCamp, "Using Python and Excel for Data Science," [Online]. Available: https://www.datacamp.com/community/tutorials/python-excel-tutorial. [Accessed 2019].

[49] A. Rhode, "MicroCFD: Computational Fluid Dynamics Software and Consulting," [Online]. Available: http://microcfd.com/index.htm. [Accessed 2019].

[50] M. Kumar, M. Kannan and V. Kumar, "Analysis of Shock Over NACA 66-206 at Supersonic Regime," *Advances in Aerospace Science and Applications,* vol. 3, no. 2, pp. 125-130, 2013.